Chapter 6

Spitzer-IRS Spectroscopy of Protoplanetary Disks: H_2O, OH, and Organics

Portions of this chapter will be submitted to *The Astrophysical Journal* with authors C. Salyk et al.

6.1 Abstract

We report spectral observations of 82 disks obtained with the Spitzer Space Telescope Infrared Spectrograph (IRS). Molecular emission from H_2O, OH, HCN, C_2H_2, CO_2, and H_2 is common, with detection rates for all species of $\sim$ 30–50%. Atomic emission features are also common, including H I, [Ne II], and [Ar III]. Excitation temperatures for the molecular species of $\sim$ 500 K and emitting radii of a few AU suggest an origin in the planet-forming regions of the disks. There are no strong correlations between detection rates or line equivalent widths and stellar or disk parameters. However, molecular detection rates are correlated with each other, and with disk color, in the sense that higher n_{13-30} and n_{6-13} implies fewer detections, suggesting a dependence on disk structure. Transitional disks, which, by definition, have anomalously high n_{13-30} colors, show no evidence for H_2O, OH, or organic molecules, perhaps because these molecules are easily photodissociated in the optically thin inner disk.

6.2 Introduction

The chemistry of protoplanetary disks plays a pivotal role in the development of planetary systems, of habitable planets, and of life. However, our understanding of the chemical conditions in protoplanetary disks—especially in the inner few AU where terrestrial planets form—is far from complete. In particular, there are many uncertainties about the role of water, which not only plays a crucial role in the formation of life as we know it, but also in many other processes that affect the formation and evolution of planets. For example, the location of water-ice sublimation, the so-called 'ice-line', may define a boundary within which planetary cores do not grow large enough to become gas giants. Whether or not a terrestrial planet has water may also have a significant effect on its geology, as water facilitates volcanism and plate tectonics (e.g., Regenauer-Lieb et al., 2001). And, water ice makes up the bulk of many outer solar system bodies, including Kuiper belt objects and outer-planet satellites.

For many years, the detection of water in protoplanetary disks remained elusive, with only a few definitive examples of ice (Malfait et al., 1998; Terada et al., 2007) and vapor (Carr et al., 2004) detections. Recently, however, Carr and Najita (2008) and Salyk et al. (2008) reported detections of numerous emission lines of water in high-resolution spectra from the Spitzer Space Telescope InfraRed Spectrograph (IRS) and the Keck Near Infrared Spectrograph (NIRSPEC). Based on emitting temperatures and line shapes, these lines appeared to originate in the disk atmospheres over terrestrial-planet forming radii.

The robust detections of water in protoplanetary disks, made possible largely by optimized high dynamic range observing strategies and data reduction routines (Carr and Najita, 2008), mark a turning point in our ability to study water's role in the early solar system. However, because water is involved in many complex chemical and physical processes in the disk, water emission can also be used to probe other disk processes. For example, water is destroyed by photodissociation and by high levels of ionization (Jonkheid et al. 2006, 2007), and so water abundances may reflect the disk irradiation environment. Because water condenses at relatively small disk radii ($\sim$ a few AU for Sun-like stars), water vapor may be driven outward by vapor pressure differences, while water ice is carried inwards by planetesimals. Hence, water abundances may reflect radial transport and planet formation timescales. Finally, the strength of water emission lines depends upon the disk structure as a whole, including the gas temperature structure, vertical transport timescales, and the degree of dust settling/grain growth.

One way to disentangle the many factors that effect water abundances and water line emission strengths is to observe a large sample of disks, and look for trends predicted by the processes described above. Here we report characteristics of disks observed during a focused high S/N program 'Water & Organics in Disks' (PI: John Carr, PID: 50641), that builds upon earlier programs, now available in the Spitzer archive, including the c2d legacy program (Evans et al., 2003) and programs P20363 (PI: J. Carr) and 30300 (PI: J. Najita). Information about the c2d program can be found in Evans et al. (2003). Program 50641 was designed to study water and organics in disks at high S/N ($\gtrsim 300$ for most disks) across a large range of disk and stellar parameters, and includes disks in the Serpens, Perseus, Taurus, Chameleon, Lupus and Ophiuchus clouds. The observed spectra included water emission, as well as solid-state features, atomic transitions, and emission from several other molecules (including C_2H_2, CO_2, and HCN). Below we report detection statistics for water and other spectral features in our disk sample, and discuss implications for disk structure and evolution.

6.3 Observations

The complete list of targets included in this study can be found in Tables 6.1 and 6.2. Information about the c2d IRS observations can be found in the c2d Spectroscopy Explanatory Supplement (Lahuis and Kessler-Silacci, 2006). Program 50641 targets were observed in 2008 in standard IRS Staring mode, with a minimum of 10 cycles on target. Dedicated sky exposures in an off-position were also obtained to remove hot pixels and properly subtract background noise. Most targets were observed in both the Short-High (SH) and Long-High (LH) modules. Exceptions are RY Tau, IQ Tau, AS 205, and RNO 91, which were only observed in LH, as high S/N SH data had already been obtained. Exposure times varied with the goal of achieving S/N ~ 300.

6.4 Data Reduction

Data were reduced with our own IDL routines, along with the IRSFRINGE package (Lahuis et al., 2007), using a procedure similar to that described in Carr and Najita (2008). We began with IRS droop-corrected, non-flat-fielded basic calibrated data (BCD) from the Spitzer Science Center IRS pipeline. We created average on and off frames, subtracted off from on, and then divided by a flat field. In order to reduce noise caused by edge-effects, pipeline flat-fields were first divided by a low-order polynomial fit in the spectral and spatial directions. Pixel values were excluded from the average if they deviated from the mean value for that pixel by more than 5 times the standard deviation. Noisy or bad pixels (with noise greater than 2 times the average noise) were also removed from the averaged frame via interpolation. Spectra were then extracted from the 2D data frames using value-weighted centering and a 3 pixel aperture, and wavelength-calibrated using an IRS wavelength map.

Science target spectra were divided by standard star spectra taken from the IRS calibration program, and reduced in the same manner. Division by a standard star helps to remove some fringing from the science spectrum, but its efficacy varies due to pointing differences between the source and standards. Using a suite of standards, we identified the frames that produced the best results. Some residual fringing remained after this step, and was carefully removed using the IRSFRINGE package. Orders were then combined, using noise values to weight overlap regions. Finally, the set of complete science/standard pairs that produce the best results were averaged together to produce the final spectrum.

For most of the analyses presented in this work, we used continuum-subtracted spectra. Proper removal of continuum emission (and solid-state features) can be difficult, because the noise is not easily distinguishable from the ubiquitous molecular emission features for data such as these in which the spectral lines are unresolved. We adopted the following procedure, which deals well with complex spectra, and consistently yields a good by-eye match to the continuum. We began with a SH or LH spectrum, and identify a smooth part of the spectrum. Using this section, we subtracted a second-order polynomial fit, and then calculated an outlier-free standard deviation (SD) for all points less than 4 standard deviations from the mean. We then smoothed the entire spectrum over 60 pixels, and subtracted 2.5 times the SD. If strong crystalline silicate emission or ice absorption was present, we smoothed the spectra in the vicinity of the features over only 5 pixels. Finally, SH and LH orders were combined. For disks in the high S/N program, no order overlap corrections were necessary. For a few disks with obvious order overlap issues from the c2d program, we adjusted according to the median value of the spectra near the overlap.

Example continuum determinations are plotted in Figure 6.1.

6.5 Results

6.5.1 Overview and Detection Statistics

The continuum-subtracted spectra contain a variety of emission features from H_2O and other gaseous molecules, as well as several atomic emission lines. In Figure 6.2, we show the complete spectrum of GQ Lup—a source which displays emission from H_2O, OH, HCN, C_2H_2, [Ar III] (21.832 μm), and H I ($n = 7 \rightarrow 6$; 12.372 μm)—along with a molecular emission model (discussed in Section 6.5.4). In Figure 6.3, we show spectra from 7 disks in the 13.5–19 μm range, showing the range of line strengths observed. The great majority of the emission features are from H_2O. Each feature is typically a blend of 2 or more transitions, and lineshapes are not spectrally resolved at R=600. Additional prominent emission features in many of the spectra are [Ne II] (12.814 μm) and H_2 (S(2); 12.279 μm). Other emission features are seen with less frequency in some spectra, but analysis of additional lines will be left for future work. In this work, we focus on H_2O, OH, and organics and only briefly discuss emission from H I, [Ar III], [Ne II] and H_2, in the context of their relationship to the other molecules.

There is significant variety in the occurrence of emission features from source to source. In Figure 6.2, one can see the contrast between a source with many molecular features (GQ Lup) and one with no detectable molecular features (CS Cha). In Figure 6.4 we show H_2O detections and non-detections as a function of signal-to-noise ratios (S/N) in the Short-High and Long-High modules, and demonstrate that these detections are not limited by S/N, except, perhaps for S/N<30. (Note that these S/N estimates are computed empirically from the spectra and will be underestimates of the true S/N if the spectra have real structure.) This result also holds true for the other molecular and atomic detections.

A summary of detection rates can be found in Table 6.3. Detection rates for H_2O, OH, and organics range from 35–49% for the sample as a whole. In Figure 6.5 we show the detection rates as a function of spectral type. We find that molecular emission is more common from disks around G, K and M stars than from B and A stars, but that the differences are only marginally statistically significant, because of the small number of early-type stars in our sample. It has been previously reported from analyses of low-resolution spectra that HCN is more common around *sun-like* (K1–M5) stars than *cool* (M5–M9) stars (Pascucci et al., 2009). With only two cool stars in our sample, we can not reliably confirm or disprove this hypothesis. Neither HCN nor C_2H_2 are detected in our cool sample, which is consistent with the low detection rates of both species found by Pascucci et al. (2009). However, we find significantly higher detection rates of HCN and C_2H_2 in our sun-like star sample than was reported in Pascucci et al. (2009), suggesting that either our samples are different, or that low-resolution spectra can result in underestimates of HCN occurrence by a factor of ~ 2, and C_2H_2(generally the weaker feature) by a factor of ~ 5.

Our sample includes eight transitional disks—disks in which an inner gap has been significantly depleted of small dust grains (Koerner et al., 1993; Calvet et al., 2002). It has been shown that many transitional inner disks contain significant amounts of gas in the form of CO (Najita et al., 2003; Rettig et al., 2004; Salyk et al., 1999, (in press), with the group of gas-rich inner disks including at least four in our sample—GM Aur, HD 135344, LkHα 330, and UX Tau A. However, we see no H_2O, OH, or organics in any transitional disk. In Table 6.3 we compare detection rates between transitional and nontransitional disks, and also calculate the probability of getting the observed transitional detection rate in a sample of eight disks, assuming they are picked at random from the non-transitional-disk population. There is a reasonable probability of obtaining the observed detection rates for H I, [Ne II], and H_2, so the two samples do not have significantly different detection rates of these species. However, for H_2O, OH, and organics, the transitional disk sample is not consistent with the non-transitional sample.

Using the results presented in Table 6.4, we search for relationships amongst detected species, and between detected species and stellar and disk parameters. In the upper-right quadrant, we show the p-value associated with the slope of a linear regression of the two parameters. In the lower left quadrant, we show the p-value for obtaining a χ^2 value at least as high as is observed, using the following procedure: We assume the actual detection rates of the two species (X and Y) are given by their observed detection rates. We then compute the expected number of matching pairs (X detected:Y detected or X not detected:Y not detected), the expected number of nonmatching pairs, and compute χ^2 using these values and the observed numbers of matching and nonmatching pairs. In both cases, a low probability implies that the relationship between the two species (or the species and stellar/disk parameter) is stronger than would be predicted by chance alone.

We find only two possible correlations between stellar/disk parameters and line detections. Not surprisingly, the H I feature in our spectra correlates with the strength of Hα, most likely because both of these features, like other hydrogen recombination lines, are created in magnetospheric accretion columns (e.g., Hartmann et al., 1994). There is also a possible relationship between stellar mass and the presence of C_2H_2. In contrast, the detection rates are strongly related to each other, in many cases. H_2 may also be correlated with some species, including H_2O, HCN, C_2H_2, and [Ar III]. The strongest correlations are found for the presence of H_2O, OH, HCN, C_2H_2, CO_2, and [Ar III]. Note, however, that there is significant overlap between one H_2O feature and the [Ar III] line. Although the feature has been classified as [Ar III] only when it noticeably exceeds the slab-model expectation for H_2O emission, it is possible that the contribution from H_2O is greater when non-LTE effects are taken into account. This could potentially remove the correlation between H_2O and [Ar III].

6.5.2 Colors

The shape of an SED is affected by disk structure and geometry. Disk colors are a simple way to parameterize the major features of the SED, and can be used to look for relationships between emission characteristics and disk structure. In this work, we calculate disk colors following procedures similar to those described in Furlan et al. (2006), except that we utilize fluxes at 30μm instead of 24 μm, to avoid the 23 μm silicate emission feature. Flux densities are calculated at 13 and 30 μm by integrating over the 12.5–14 and 29–31 μm regions, respectively, and then dividing by the width of the region. At 6 μm, we adopt 5.8 μm IRAC fluxes from the literature (see Table 6.5). We then use the flux densities to calculate spectral indices n_{6-13}, n_{6-30}, and n_{13-30}, where

$$n = \log\left(\frac{\lambda_2 F_{\lambda_2}}{\lambda_1 F_{\lambda_1}}\right) / \log(\frac{\lambda_2}{\lambda_1}).$$

When 6 μm fluxes are unavailable, we use spectral indices from Furlan et al. (2006) and Watson et al. (2009). The colors for our entire sample are shown in Table 6.5.

We do not find any strong correlations between single disk colors and any species detection rates. However, in the top panel of Figure 6.6, we show a possible trend for detection rates on a two-color diagram. Towards the top and right of the figure, detections are much less common. In Table 6.6 we show that the detection rates inside and outside the outlined region are indeed different in a statistically significant sense. Although we show in this figure the detections and nondetections for H_2O, the differences are also apparent for OH, the organic molecules and [Ar III], as these detections are all correlated with each other.

Low n_{13-30} values are associated with a large amount of small dust grains in the upper disk layers, while high n_{13-30} values are associated with depletion of small grains in the upper layers—either due to overall removal, or settling of small grains to the midplane (e.g., Furlan et al., 2006). In this case, the high n_{13-30} sources in the top left and top center are transitional disks, so the high n_{13-30} results from an overall depletion of disk dust grains. However, even after accounting for the transitional disks, there is a difference between Region 1 and Region 2 detection rates. Both n_{13-30} and n_{6-13} increase as disk inclination increases, so this trend could represent a relationship between detectability and disk inclination, with low inclinations being easier to detect. However, we do not see a direct relationship between disk inclination in detectability, according to Table 6.4. Another possibility is that the trend could be attributed to accretion rate, which is negatively correlated with the n_{6-13} ratio (Furlan et al., 2006). Molecular detections may correlate with accretion rate because disk atmospheres are hotter, and can more easily excite the observed transitions.

6.5.3 Equivalent Widths

In addition to studying line emission occurrences, we investigate trends associated with the strength of the emission features. In Table 6.7, we show equivalent widths calculated for all detected emission features. Equivalent widths are calculated by integrating over the following wavelength regions (in μm): H I (12.330–12.430); H_2O(12.325–12.427 and 32.907–33.102); OH (18.755–18.909); HCN (13.957–14.065); C_2H_2(13.687–13.719); CO_2 (14.923–14.994); [Ne II] (12.780–12.845); [Ar III] (21.820–21.850); H_2 (12.230–12.305). To compute error bars, we use the standard deviation of the flux in a quiescent region—usually between 10.263 and 10.644 μm in the short-high module, and between 24 and 24.3 or 26.1 and 26.4 μm in the long-high module. Prior to computing equivalent widths for all molecules besides H_2O, we first subtract a best-fit H_2O emission model (described in Section 6.5.4).

In Table 6.8 we show the relationships between stellar and disk parameters and equivalent widths, as well as between equivalent widths of different emission features. In this table, values above the diagonal are the correlation coefficient, R, between the two parameters. Values below the diagonal are the p-value associated with a linear regression of the two parameters. We have bolded both numbers if $\mathrm{p} \leq 0.02$. We find only two correlations between disk parameters and line equivalent widths—anti-correlations between $\log \dot{M}$ and both H_2 and C_2H_2. This relationship can be accounted for entirely by the fact that the equivalent widths of both molecules are strongly anti-correlated with the continuum flux level. Once this is accounted for, the relationship disappears; there is no relationship between line *strength* and $\log \dot{M}$.

Several correlations exist between different molecular equivalent widths. These are roughly in agreement with the detection correlations: H_2O, OH, HCN, C_2H_2, [Ne II], and [Ar III] are, to some extent inter-related. Correlations with [Ne II] may be determined by the continuum level, as [Ne II] equivalent widths are strongly anti-correlated with the continuum. Strong correlations between [Ne II] and both H I and H_2 are the result of transitional disks, for which both lines have stronger than average equivalent widths when present.

In Table 6.9, we show possible relationships between disk colors and equivalent widths. Table inputs are p-values for the slope of a linear regression of the two parameters. Strong (positive) correlations with n_{13-30} are seen for H I and [Ne II]. In both cases, this is due to the fact that transitional disks have large H I and [Ne II] equivalent widths, as well as high n_{13-30}. In Figure 6.7, we plot [Ne II] against n_{13-30}, and label the transitional disks. There is no apparent trend once these sources are removed. In Figure 6.7, we show that the relationship between [Ne II] equivalent width n_{13-30} is due to the strong [Ne II] equivalent widths for transitional disks. This, in turn, is mostly, if not entirely, due to the reduced continuum at $\sim$13 μm.

6.5.4 Models

6.5.4.1 Description of Model

To obtain a better physical understanding of the source of the disk emission, we fit the molecular emission with emission models. In this work, we use an isothermal slab approximation, in which area A, temperature T, and column density N are all free parameters. These models are the same as those utilized in Salyk et al. (2008), and assume a Gaussian local line shape with width, $\sigma = 2$ km s^{-1}. Note that the lines are not spectrally resolved, and so the true line shape is unknown.

There are many limitations to using this simple slab model. The actual disk environment is quite complex, with densities and temperatures that depend on both height and radius. The observed emission almost certainly arises from only the upper disk atmosphere (except, possibly, in the case of the transitional disks), and so the best-fit model parameters represent the flux-weighted average parameters of the upper disk atmosphere at a variety of radii. In addition, the molecular emission may not actually arise from a thermalized gas, in which case the derived column densities can be quite different from those actually present. Finally, the local turbulent velocity is unknown, yet can significantly affect the derived fit parameters (Salyk et al., 2008).

Many of the more complex issues related to line excitation and disk structure are being pursued with more complexing radiative transfer modeling (Meijerink et al., in prep). Here, we use the slab models to understand the bulk properties of the emitting atmospheres, to investigate the variety of emission observed, and to estimate molecular abundance ratios. By focusing on abundance ratios, rather than abundances, we may be less sensitive to some of the limitations mentioned above.

6.5.4.2 H_2O Models

We fit the H_2O emission spectra by iterating over a grid of T, A, and N. T ranges from 200–1200 K with 100 K spacing, A ranges from $4 \times 10^{-4} - 4 \times 10^{2}$ AU^2 with log spacing of ~ 0.6, and N ranges from 10^{16}–10^{22} cm^{-2} with log spacing of ~ 0.3. Best fit models were chosen to minimize the sum of squared residuals between data and model.

Best-fit model parameters are listed in Table 6.10 and shown graphically in Figures 6.8 and 6.9. Typical allowed ranges for the fit parameters are $\sim$ 300 K in temperature, a factor of $\sim$ 100 in density, and a factor $\sim$ 3 in area, assuming the reduced χ^2 of the best model is 1, and using a 95% confidence interval. However, these error ranges are larger than the true uncertainties, as can be seen in the histograms of Figure 6.8. This may be because the parameters are not independent, but instead correlated with each other, as can be seen in Figure 6.9. True error bars are likely about a factor of 2 smaller.

In general, H_2O emission models are consistent with temperatures of $\sim$ 500 K, densities of $\sim 5 \times 10^{18}$ cm^{-2}, and emitting areas of a few AU^2. These results suggest that the emission arises in the warm, inner few-AU region of the disk. Peak optical depths for the strongest lines in the model exceed $\sim$ 1000, which implies that $H_2\,^{18}O$ may be detectable, and therefore accessible for studies of isotopic fractionation in disks.

6.5.5 Other Molecular Models

In addition to H_2O we have fit emission from OH, C_2H_2, CO_2, and HCN. For all molecular fits, we first subtracted the best-fit H_2O emission model, if H_2O was present. To fit the OH emission, we use the same procedure as was used for H_2O. For C_2H_2 and CO_2, it was not possible to simultaneously fit the three model parameters, because there is only a single Q-branch feature detectable at the resolution of the Spitzer IRS, and both density and temperature affect the model in similar ways (see Figure 6.11). It may be possible to distinguish the effects of temperature and density differences for HCN, but we leave this as future work. Therefore, for all molecules besides OH, we assumed the same emitting area and temperature as for H_2O, and fit only for column density.

The results of these model fits are shown in Table 6.10. Model fits typically yield densities of 5×10^{15} for CO_2, and $10^{16}\,\mathrm{cm}^{-2}$ for HCN. C_2H_2 densities range from $\sim 10^{15}$–$10^{16}\,\mathrm{cm}^{-2}$. However, in many cases, the best-fit model appears, by eye, to have overestimated the strength of the emission feature (see Figure 6.2). This is due to the fact that the Q-branches are actually too broad to be properly fit by the constrained values of temperature and density. Therefore, either the model temperatures or the model densities would need to be increased, and model areas would need to be reduced accordingly. Nevertheless, we show ratios of molecular column densities relative to H_2O are in Figure 6.10, and compare to both previous results (Carr and Najita, 2008), disk models (Markwick et al., 2002) and ices (Gerakines et al., 1999; Whittet et al., 2007; Pontoppidan et al., 2008a). Error bars show the standard deviation of the entire sample. Note that the large difference in density ratios between previous results for AA Tau (Carr and Najita, 2008) and this work (which includes AA Tau in the sample) can be primarily attributed to the fact that the areas in the previous work were allowed to vary, and found to be smaller than for H_2O by factors of 3–10 for CO_2, HCN, and C_2H_2. Differences for OH arise from differences in best-fit temperatures. This issue is being investigated further, and will be addressed in more detail in future work. Our results appear nearly consistent with disk models at 1 AU, but are significantly lower than ratios found in YSO and cloud ices.

OH model-fitting results are shown in Figure 6.8. The OH emission appears to be best-fit with very high emitting temperatures—in the range of 600–1200 K. 1200 K is the upper end of our temperature grid, so emitting temperatures may be even higher. Densities are typically $\sim 10^{15}$, 3–4 orders of magnitude lower than that of H_2O, while emitting areas are typically factors of ~ 5 larger than for H_2O. The need for both large emitting areas (i.e., large radii) and high temperatures is inconsistent with disk structure, in which temperatures drop with radius. This may mean that the OH we observe is not in thermodynamic equilibrium. Mechanisms for non-LTE excitation of OH include UV-pumping by the central star and the photodissociation of H_2O followed by 'prompt' emission (Bonev et al., 2006).

6.6 Discussion

When observed at sufficient spectral resolution and with high S/N, emission lines from H_2O, OH, and organics are seen with high frequency around young low mass (G,K, and M) stars. Detection rates for all molecules are typically $\sim 40\%$, and detections and strengths of each species are correlated with each other. Because the molecules do not share a common chemical origin, the prominence of emission lines may be more strongly influenced by the disk environment than by the rates of production and destruction.

Because H_2O condenses at only a few AU, the H_2O content of the inner disk can potentially be affected by the rates of outward vapor diffusion and inward ice migration followed by sublimation (Ciesla and Cuzzi, 2006). The fact that H_2O emission does not appear unique in any way suggests that the H_2O emission lines are not significantly affected by this process.

Unfortunately, there are few obvious trends between detection rates or line strengths and stellar or disk parameters, although we will continue to investigate this issue. There is, however, a trend of decreasing detectability of most molecular species with increasing n_{6-13} and n_{13-30}, which could be due to inclination effects, settling, accretion luminosity, or some combination of these.

One the most unambiguous results of this study is a notable difference in the spectra from classical and transitional disks. No H_2O, OH, or organics are detected in our observations of transitional disks, although the presence of CO and [Ne II] in many transitional disks means that their inner regions do contain significant quantities of gas. A possible reason for the lack of emission may be that because the disk is optically thin, the molecules are not well shielded from the strong radiation field of the central star. CO (and H_2) on the other hand, can self-shield.

Simple slab models, with temperature, emitting area, and column density as free parameters, do a reasonable job of reproducing the major features of the observed spectra. These models suggest that the emission arises from within a few AU of the central star, consistent with both the best-fit emitting areas and temperatures. Molecular ratios are roughly consistent with those predicted by disk chemical models, and lower than those found in YSO and cloud ices, but differences between this work and previous studies highlights potential systematic uncertainties in model parameters.

Two important limitations to studies utilizing slab models include the degeneracy of parameters, and the unknown local velocity. Both of these issues could be resolved with higher-resolution data; line shapes depend on both the local line broadening and the area of origin for the emission. A survey of 3μm H_2O and OH emission from disks at higher resolution (R$\sim$25000) is currently being pursued with NIRSPEC on the Keck II telescope (Salyk et al., in prep).

There are other apparent limitations to the slab models. The H_2O models do not reproduce well the short-wavelength emission lines, below $\sim 14\ \mu$m, and do not always produce the correct flux for all lines. In addition, OH emission is consistent with very high temperatures and large emitting areas, which could suggest that these features are not thermally excited. A disk model including radiative transfer and nonthermal excitation mechanisms fits much better the emission features (Meijerink et al., in prep). The relationship between the fit parameters in the slab and in a full disk model is not known, but is currently being investigated.

The set of spectra presented in this work represents a rich new dataset to explore disk structure and chemistry. As it was designed for studies of disk gas, it provides an important complement to the many studies that have been made of the solid-state components of disks. First results show that molecular emission is common, and may be related to disk structure. H_2O emission shows no evidence of the effects of radial transfer, and OH emission suggests that an understanding of nonthermal excitation could be important for the intepretation of disk emission. Future work will explore particular species in more detail, and include searches for additional atomic and molecular emission. In addition, radiative transfer models are currently being created to investigate in more detail the origin of the emission lines, and the conditions in disk atmospheres, including turbulent broadening and non-LTE gas heating.

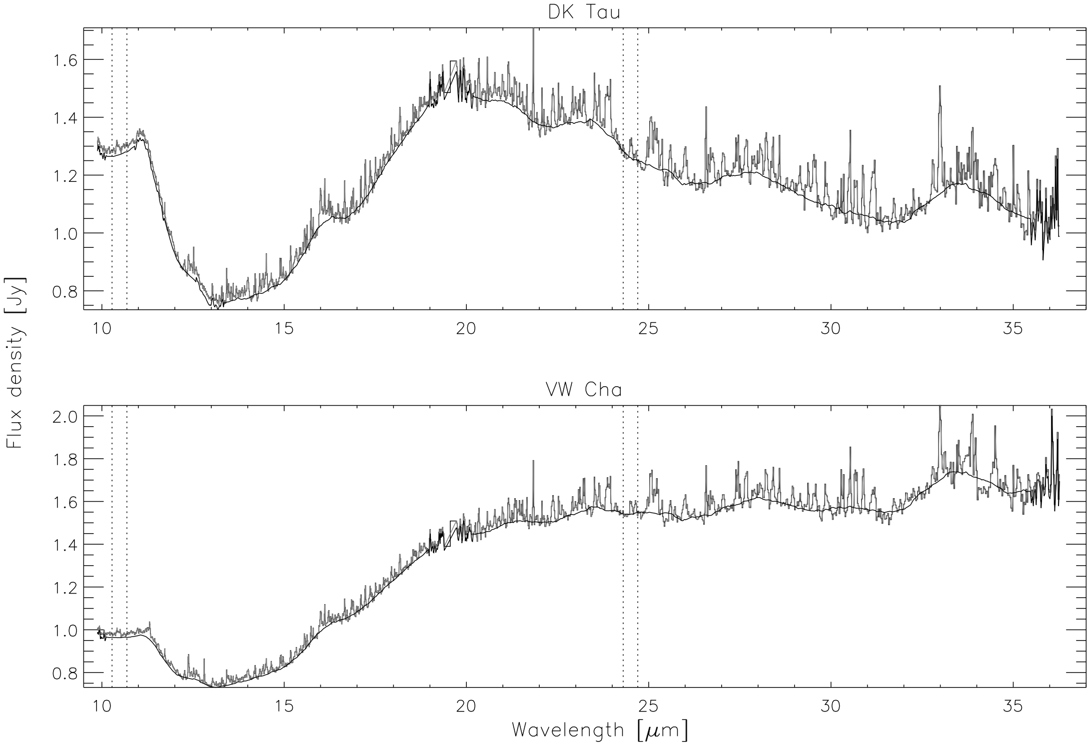

Figure 6.1: Continuum determination for two disks. Samples of continuum determination for two disks. Data are shown in gray, and continuum (described in text) in black. Regions between the dotted lines show where the standard deviation was calculated.

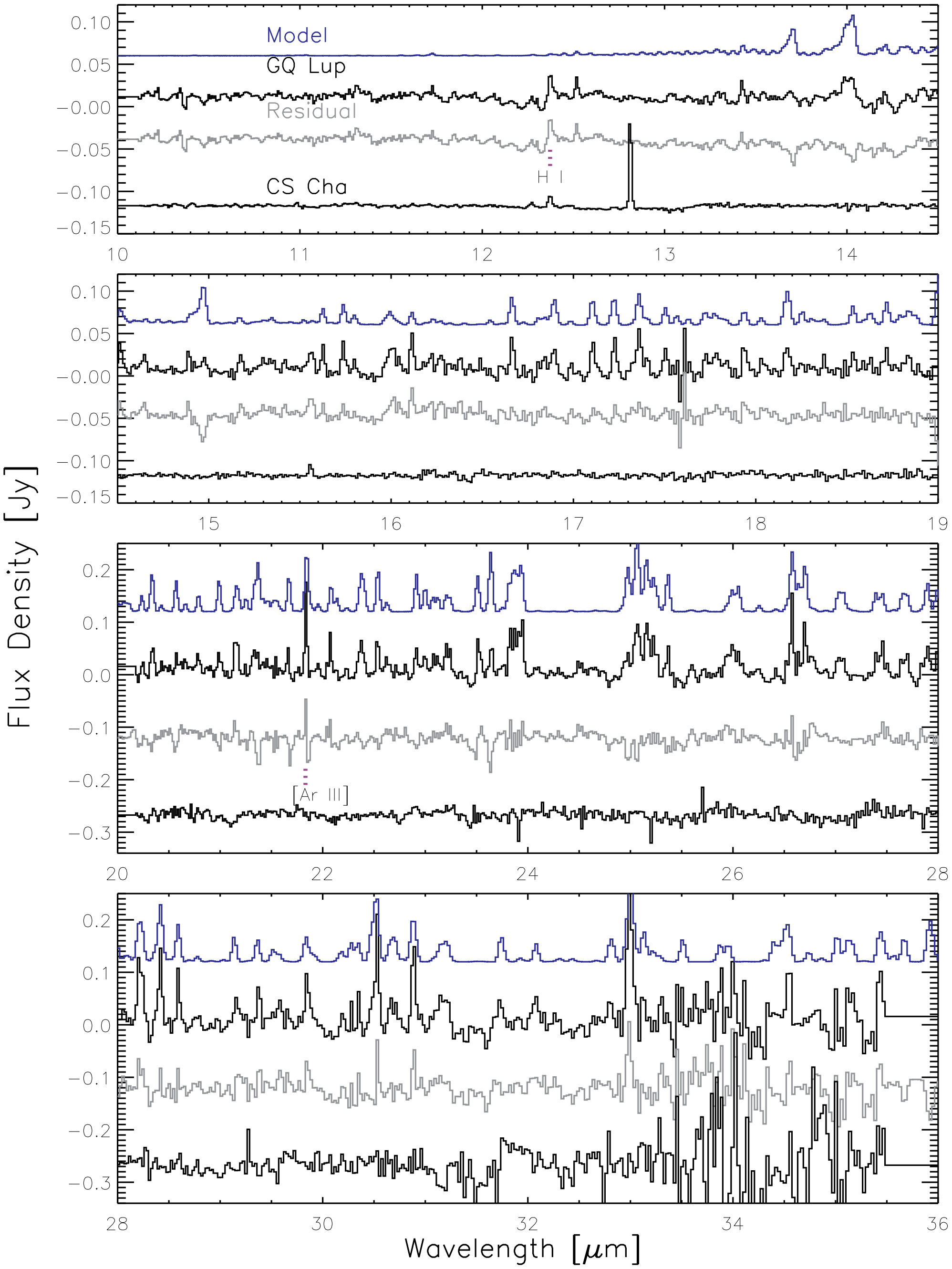

Figure 6.2: Data, best-fit molecular models, and residuals.

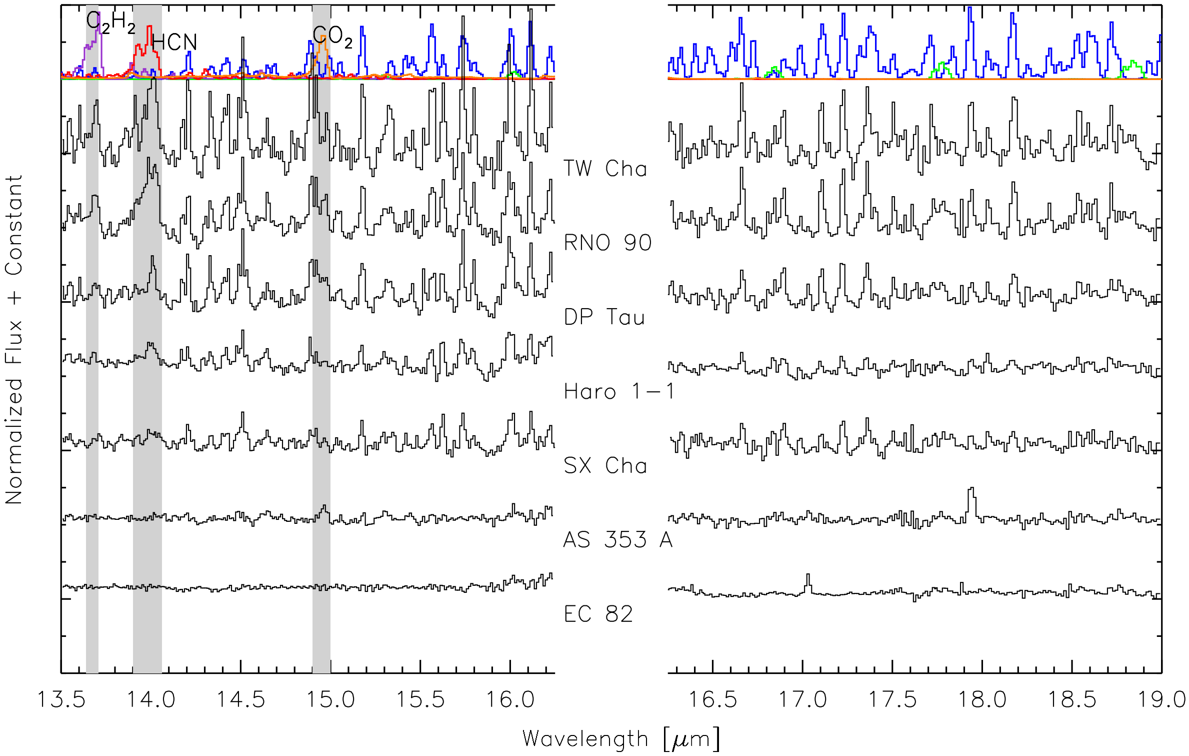

Figure 6.3: Spectra for 7 disks in our sample, showing a variety of emission line strengths. Plotted above are emission spectra expected for H_2O, HCN, CO_2, and C_2H_2.

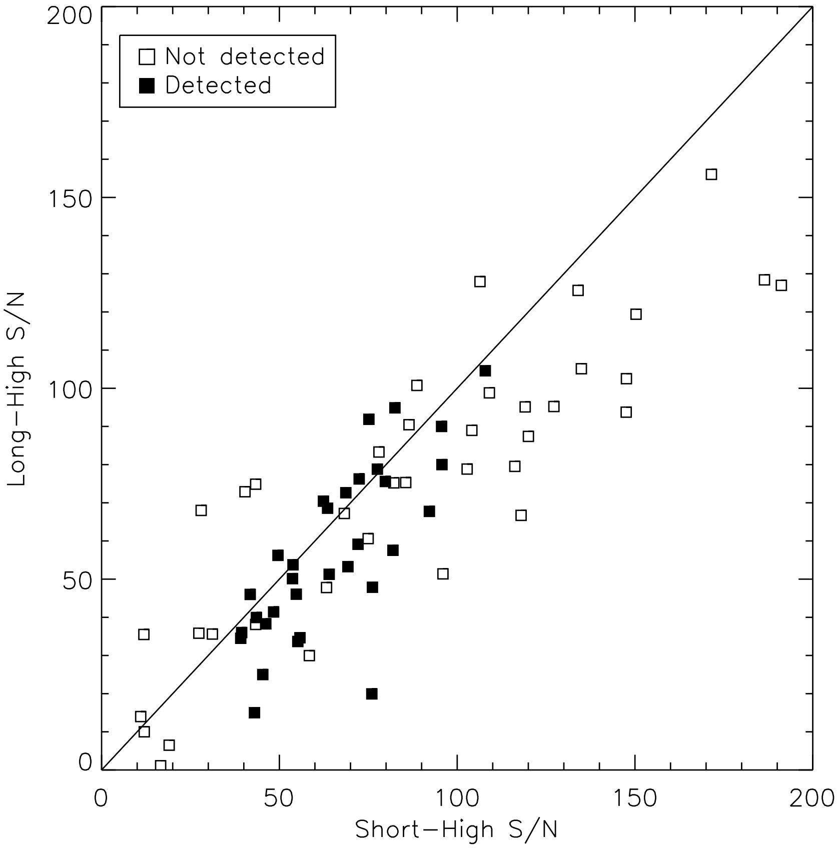

Figure 6.4: Detections and non-detections as a function of S/N in the Short-High and Long-High modules. S/N ratios are taken as Median/σ. σ is computed after subtraction of a best-fit H_2O model.

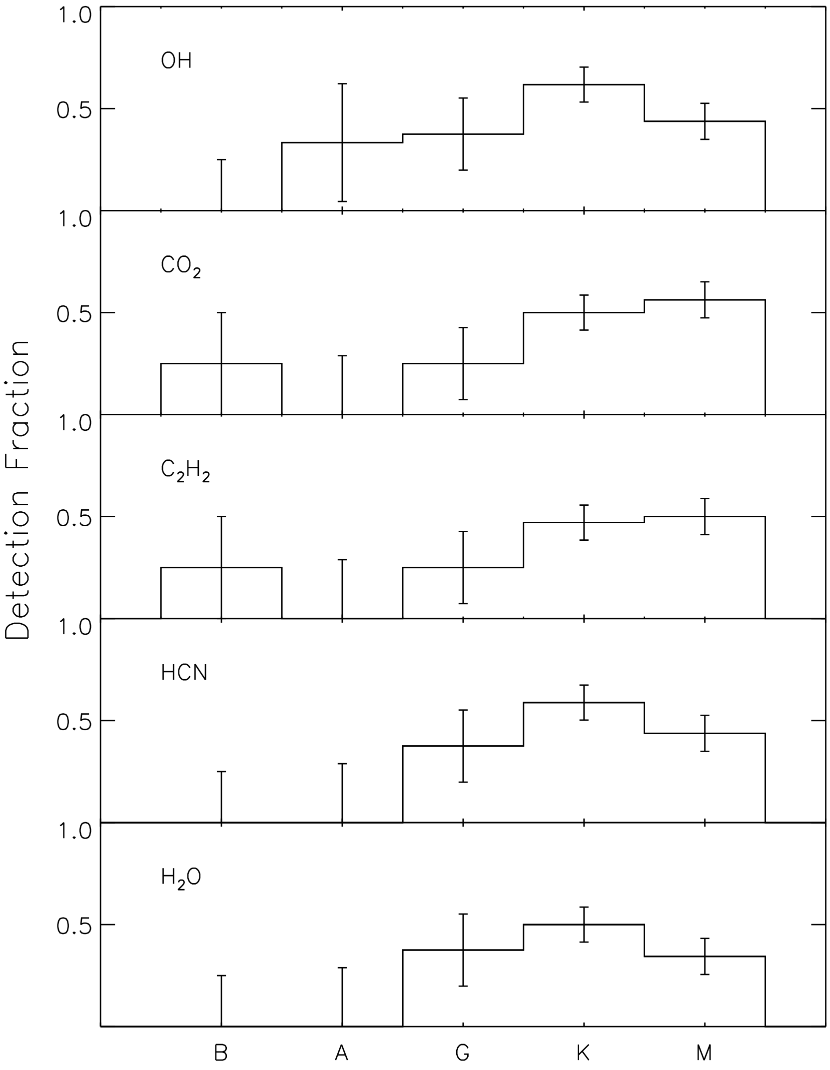

Figure 6.5: Detection fractions as a function of spectral type.

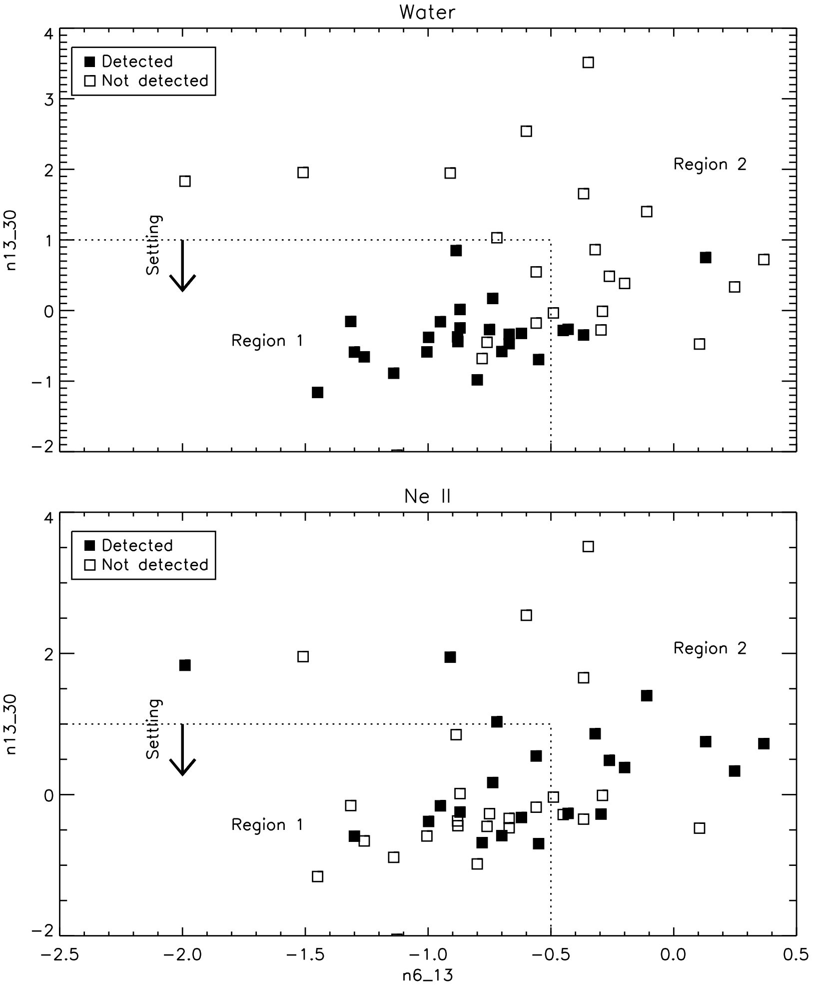

Figure 6.6: Detections and non-detections of H_2O and [Ne II] on a color-color diagram. A two-color plot showing detections and non-detections of H_2O and [Ne II]. Note that settled sources are more likely to have H_2O emission, but are not more likely to have Ne II emission.

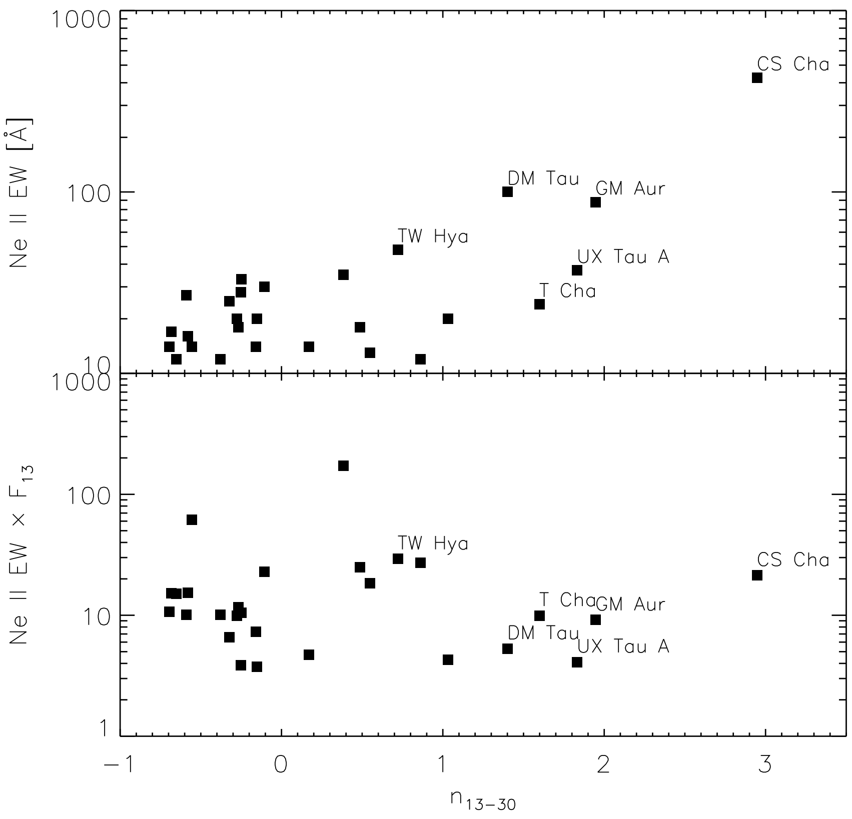

Figure 6.7: Ne II equivalent width versus n_{13-30} color. Sources at the extreme upper right are labeled. Note that the majority of these are transitional disks.

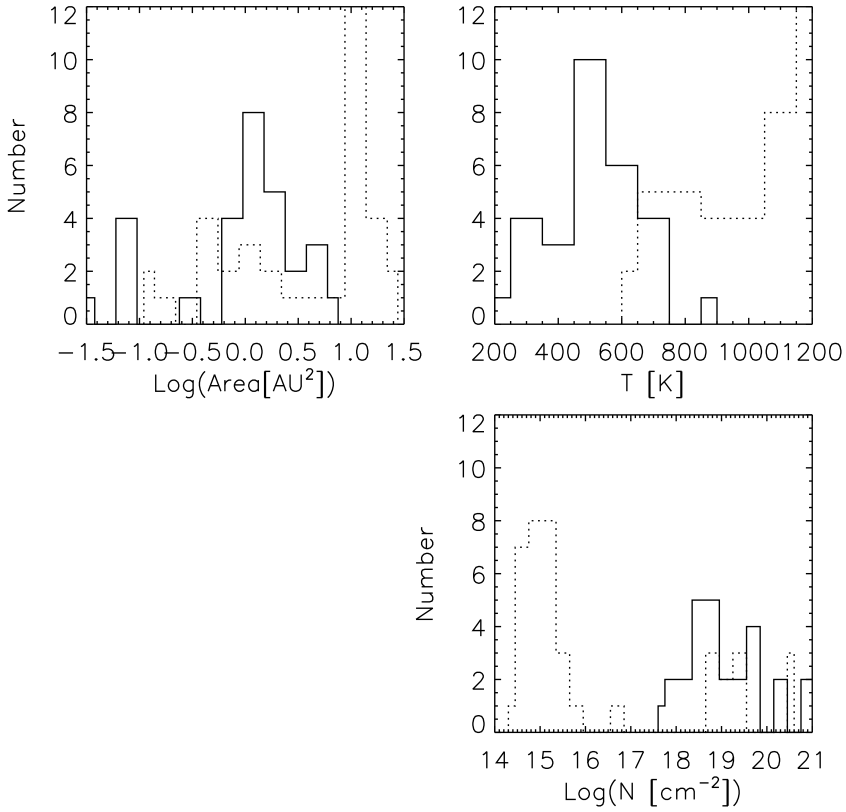

Figure 6.8: Histogram of H_2O (solid lines) and OH (dashed lines) model-fit parameters

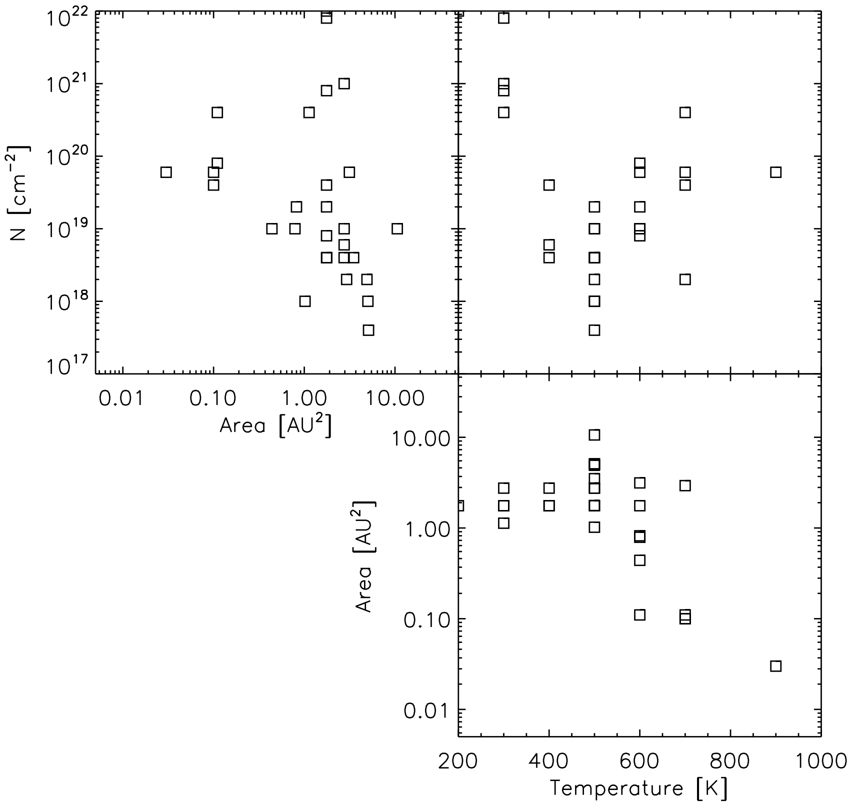

Figure 6.9: Correlations between H_2O model-fit parameters. Note that emitting areas are typically a few AU^2, and temperatures are typically 400–600 K, suggesting that the H_2O resides in the inner disk. Also note the strong anti-correlation between temperature and emitting area.

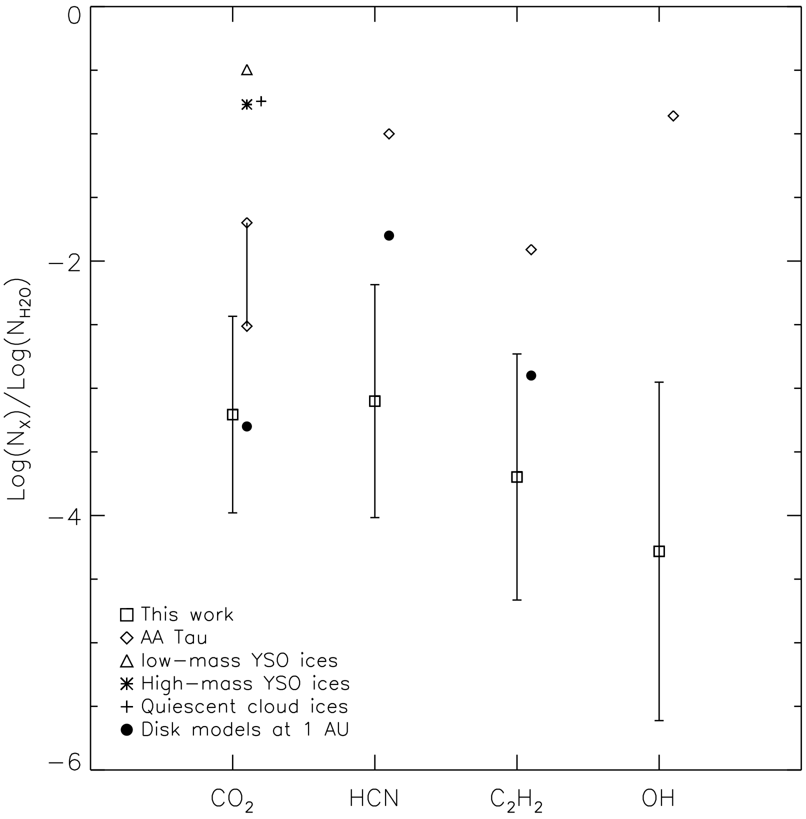

Figure 6.10: Molecular ratios from this work, compared to previous results and other environments. References are: for AA Tau, (Carr and Najita, 2008), low-mass YSO ices (Pontoppidan et al., 2008b), high-mass YSO ices (Gerakines et al., 1999), and quiescent cloud ices (Whittet et al., 2007).

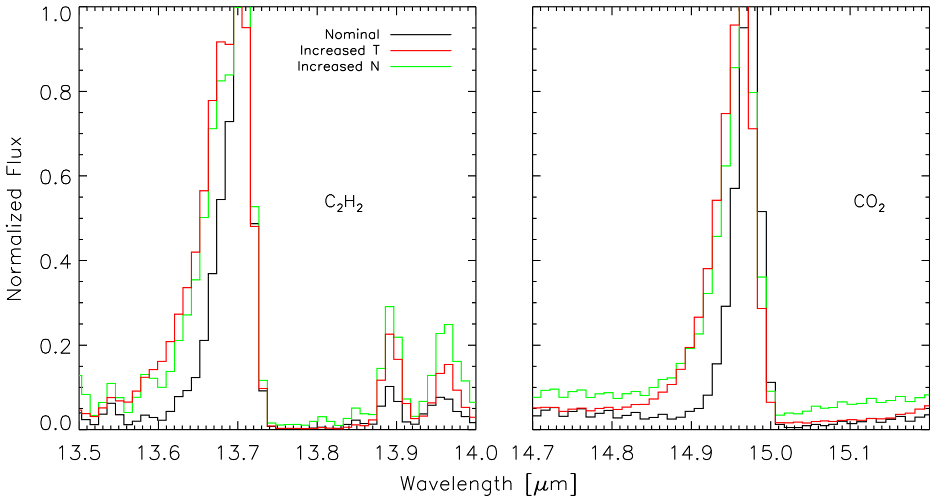

Figure 6.11: Sample model results for CO_2 and C_2H_2. Note that increased temperatures and column densities affect the model output in similar ways. For both molecules the nominal model has $T = 400\,\mathrm{K}$, and the high-T model has $T = 900$ K. For C_2H_2, N is increased by a factor of 60 for the high-N model, while for CO_2 it is increased by a factor of 6000.

Table 6.1: Stellar Parameters

Star	d [pc]	SpT	ref	Lx [^{1}]	ref	$M_\star$ [$M_\odot$]	ref	$L_\star$ [$L_\odot$]	ref	A_V	ref
AA Tau	140	K7	6,23	1.24	26	0.67	12	0.98	12	1.75	23
AS 205 A	160	K5	44	···	···	1.50	44	7.10	44	2.90	44
AS 353 A	200	K3	22	···	···	···	···	···	···	2.10	44
BF Ori	400	A5–F6	36	···	···	···	···	···	···	0.55	55
BP Tau	140	K7	6,23	1.36	26	···	12	0.95	12	1.00	23
CHXR 30	178	K7–M1	38	1.91	4	···	···	···	···	···	···
CI Tau	140	K7	6,23	0.20	26	0.70	12	0.87	12	2.00	23
CoKu Tau/4	140	M1.5	6,23	<0.21	42	0.43	56	0.68	56	3.00	23
CS Cha	178	K4	3	1.00	21	1.20	21	1.10	21	0.85	55
CW Tau	140	K3	6,23	2.84	26	1.40	12	1.10	12	2.75	23
CY Tau	140	M1	6,23	0.19	26	0.48	12	0.50	12	1.70	23
DE Tau	140	M1–M2	6,23	<0.29	42	0.44	12	1.21	12	1.20	23
DG Tau	140	K5–M0	27	0.25	26	0.56	12	1.70	12	1.60	23
DK Tau	140	K7	6,23	0.92	26	0.65	12	1.30	12	1.30	23
DL Cha	178	M6	36	···	···	···	···	···	···	···	···
DL Tau	140	K7	6,23	<0.31	42	0.76	33	0.77	12	1.50	23
DM Tau	140	M1	6,23	0.18	26	0.62	12	0.30	12	0.72	23
Do Ar 24E	160	K7–M0	25	0.50	15	0.47	41	1.26	41	2.90	25
Do Ar 25	160	K3–M0	10	0.25	15	0.49	41	1.35	41	2.90	7
DO Tau	140	M0	6,23	···	···	0.57	12	1.38	12	2.05	23
DP Tau	140	M0	6,23	0.10	26	0.60	12	0.20	12	0.60	23
DR Tau	140	K7	6,23	<0.64	42	0.55	12	2.50	12	1.20	23
EC 82	260	M0	36	···	···	···	···	···	···	···	···
EX Lup	150	M0	30	···	···	0.59	30	0.39	30	0.00	55
FN Tau	140	M5	35	< 0.37	42	0.11	35	1.00	12	1.35	23
FT Tau	140	cont	6,23	<0.22	42	···	···	1.30	56	···	···
FX Tau	140	M1	6,23	0.50	26	0.44	12	1.02	12	2.00	23
FZ Tau	140	M0	6,23	0.64	26	0.57	56	1.08	56	3.70	23
GI Tau	140	K7	23	0.83	26	0.91	12	1.00	12	2.30	23
GK Tau	140	K7	6,23	1.47	26	0.57	12	1.40	12	1.15	23
GM Aur	140	K7	6,23	<0.55	42	0.72	12	0.70	12	1.21	23
GQ Lup	150	K7–M0	30	···	···	0.80	48	0.80	48	0.50	48
GW Lup	100	M2–M4	30	···	···	0.46	30	0.23	30	0.00	55
Haro 1-16	125	K2–K3	36	···	···	···	···	···	···	···	···
Haro 1-17	125	M2.5	36	···	···	···	···	···	···	···	···
Haro 1-1	125	K5–K7	36	···	···	···	···	···	···	1.70	55
Haro 1-4	125	K6–K7	36	···	···	···	···	···	···	···	···
Haro 6-13	149	M0	6,23	0.80	26	0.55	12	2.10	12	11.90	23
HD 101412	160	B9.5	36	···	···	···	···	···	···	0.56	55
HD 135344	84	A0–F4	36	···	···	1.50	24	8.00	24	0.30	24
HD 98922	540	B9	24	···	···	5.00	24	···	24	0.30	24
HK Tau	140	M0.5–M	6,23	0.08	26	0.55	12	0.56	12	2.70	23
HN Tau	140	K5	6,23	0.15	26	0.59	12	0.25	12	1.50	23
HQ Tau	140	···	···	5.32	26	···	···	5.37	12	···	···
HT Lup	145	K2	30	···	···	1.57	30	1.45	30	1.45	55
IM Lup	140	M0	30	···	···	1.00	43	1.30	30	0.98	55
IQ Tau	140	G0–M0	6,23	0.42	26	0.54	12	0.88	12	1.44	23
LkCa 8	140	M0	36	···	···	···	···	···	···	···	···
LkHa 270	250	K2.5	22	···	···	···	···	···	···	···	···
LkHa 326	250	G-M0	36	···	···	···	···	···	···	···	···
LkHa 330	250	G2–G3	22	···	···	···	···	···	···	···	···
LkHa 348	260	cont	22	···	···	···	···	···	···	···	···
RNO 15	250	···	···	···	···	···	···	···	···	···	···
RNO 90	140	G5	36	···	···	···	···	···	···	···	···
RNO 91	140	···	···	···	···	···	···	···	···	···	···
ROXs 42C	125	M	36	···	···	···	···	···	···	···	···
ROXs 43A	125	G0–G8	36	···	···	···	···	···	···	···	···
RR Tau	160	B8–A5	36	···	···	2.50	24	37.00	24	1.10	24
RU Lup	140	K7–M0	30,28	···	···	1.00	28	0.42	28	0.10	28
RW Aur	140	K1–K3	56,22	···	···	1.34	56	1.70	56	0.50	23

Continued on Next Page...

Table 6.1 – Continued

Star	d	SpT	ref	Lx	ref	$M_\star$	ref	$L_\star$	ref	A_V	ref
RY Lup	150	K0–K4	30	⋯	⋯	1.19	30	1.30	30	0.65	55
SR 9	125	K4–M2	25	2.51	15	0.60	41	1.90	41	2.50	25
St 34	140	M3	31	⋯	⋯	0.37[2]	57	⋯	⋯	⋯	⋯
SU Aur	140	G1–G2	6,23	9.46	26	2.65	12	9.90	12	0.90	23
SX Cha	178	M0.5	36	< 0.32	21	0.80	21	0.30	21	1.12	21
SY Cha	178	M0	36	0.16	21	0.80	21	0.30	21	0.21	21
Sz 18	178	M2.5	37	⋯	⋯	⋯	⋯	⋯	⋯	⋯	⋯
Sz 50	178	M3	36	3.02	4	⋯	⋯	⋯	⋯	⋯	⋯
T Cha	66	G2-G8	36	⋯	⋯	⋯	⋯	⋯	⋯	⋯	⋯
TW Cha	178	M0	36	1.00	21	1.00	21	0.90	21	2.99	21
TW Hya	56	K7	10	2.00	10	0.77	28	0.17	28	0.00	55
UX Tau A	140	K2	6,23	0.95	42	1.49	12	2.70	12	0.70	23
UY Aur	140	⋯	⋯	⋯	⋯	⋯	⋯	⋯	⋯	⋯	⋯
V1331 Cyg	500	A8-G5	40	⋯	⋯	⋯	⋯	⋯	⋯	2.40	40
V710 Tau	140	M0.5	6,23	1.38	26	0.42	56	1.10	56	1.90	23
V853 Oph	125	M1.5	36	⋯	⋯	0.42	41	1.05	41	⋯	⋯
VV Ser	260	B1–A3	36	⋯	⋯	3.10	24	85.00	24	3.10	24
VW Cha	178	M0.5	36	9.33	21	0.60	21	3.31	21	2.39	21
VZ Cha	178	M0	36	1.26	21	0.90	21	0.30	21	0.47	21
Wa Oph 6	140	K6	7	⋯	⋯	⋯	⋯	⋯	⋯	3.50	7
WX Cha	178	K7	36	1.48	21	0.80	21	0.85	53	2.14	21
XX Cha	178	M2	36	< 28.60	46	0.70	21	0.10	21	0.61	21

---

[1] 10^{30} erg s^{-1}

[2] For each member of a spectroscopic binary

Table 6.2: Disk Parameters

Star	EW$_{H\alpha}$ [Å]	ref	$\log \dot{M}$ [$10^{-8} M_{\odot}\mathrm{yr}^{-1}$]	ref	M_d [$M_{\odot}$]	ref	i_d [°]	ref	ID*
AA Tau	37	12	-8.48/-8.19	7	0.03	6	75	33	3
AS 205 A	55–155	22,32	-6.14/-6.14	7	0.0330	8	47	7	1
AS 353 A	15–17	22	···	···	···	···	···	···	3
BF Ori	6–11	32	···	···	···	···	···	···	2
BP Tau	40–76	12,22	-7.88/-7.54	26	0.0200	6	20	50	3
CHXR 30	···	···	···	···	···	···	···	···	4
CI Tau	102	12	-7.59/-7.19	7	0.0400	6	46	7	1
CoKu Tau/4	1–2	32	< -11.00	17	0.0005	6	···	···	2,4
CS Cha	13	21	-7.92/-7.92	20	···	···	···	···	4
CW Tau	135–140	12	-8.80/-7.99	27	0.002	6	···	···	1
CY Tau	70	12	-8.86/-8.12	26	0.006	6	47	50	1
DE Tau	54	12	-7.59/-7.59	39	0.005	6	···	···	1
DG Tau	113	12	-8.40/-6.13	27,28	0.0200	6	70	16	3
DK Tau	19	12	-7.42/-7.42	26	0.005	6	···	···	3
DL Cha	···	···	···	···	···	···	···	···	2
DL Tau	105	12	-7.73/-7.17	7	0.1	6	35	7	1
DM Tau	140	12	-8.70/-8.67	7	0.014	6	32	7	4
Do Ar 24E	···	···	-8.46/-8.46	41	0.008	8	···	···	1
Do Ar 25	2	10	< -9.24	7	0.1	9	62	7	2
DO Tau	109	12	-6.85/-6.85	39	0.007	6	42	34	3
DP Tau	86	12	-8.50/-6.92	27	<0.0005	6	···	···	1
DR Tau	87	12	-6.50/-6.25	7	0.01	6	72	7	1
EC 82	5–11	32	···	···	···	···	···	···	1
EX Lup	31–43	32	···	···	···	···	···	···	1
FN Tau	16–25	12,35	···	···	0.007	35	20	35	2
FT Tau	189	31	···	···	0.05	6	60	7	1
FX Tau	10–15	26	-8.65/-8.65	26	0.0009	6	···	···	2
FZ Tau	204	12	-7.70/-7.70	56	0.002	6	···	···	1
GI Tau	15–21	26	-8.08/-8.08	26	···	···	···	···	3
GK Tau	15–35	26	-8.19/-8.19	26	0.002	6	···	···	3
GM Aur	97	12	-8.18/-8.02	7	0.057	6	54	47	4
GQ Lup	31–39	32	-8.00/-7.00	48	···	···	51	48	1
GW Lup	90–98	32	···	···	···	···	···	···	2
Haro 1-16	59–76	32	···	···	···	···	···	···	1
Haro 1-17	15	32	···	···	···	···	···	···	2
Haro 1-1	···	···	···	···	···	···	···	···	2
Haro 1-4	···	···	···	···	···	···	···	···	2
Haro 6-13	34–88	26	-7.54/-7.54	26	0.01	6	···	···	1
HD 101412	14–20	32	···	···	···	···	···	···	2
HD 135344	17	32	-8.30/-8.30	24	···	···	46	18	2
HD 98922	27	32	-5.76/-5.76	24	···	···	···	···	2
HK Tau	29–54	26	-7.65/-7.65	26	0.004	6	84	52	1
HN Tau	138–163	26	-8.60/-8.60	56	0.0008	6	···	···	1
HQ Tau	···	···	···	···	0.0005	6	···	···	1
HT Lup	3–7	32	···	···	···	···	···	···	1
IM Lup	4–8	32	···	···	0.1	43	50	43	1
IQ Tau	8	12	-8.32/-7.55	26	0.02	6	79	33	1
LkCa 8	···	···	···	···	···	···	···	···	2
LkHa 270	92	22	···	···	···	···	···	···	2
LkHa 326	···	···	···	···	···	···	···	···	1
LkHa 330	11–20	22	-8.80/-8.80	22	···	···	40	14	1
LkHa 348	301–324	22	···	···	···	···	···	···	2
RNO 15	116	32	···	···	···	···	···	···	2
RNO 90	76	32	···	···	0.0047	8	···	···	1
RNO 91	···	···	···	···	0.01	5	···	···	1
ROXs 42C	···	···	···	···	<0.005	5	···	···	2
ROXs 43A	···	···	···	···	<0.005	5	···	···	2
RR Tau	21–50	32	-6.90/-6.90	24	···	···	···	···	2
RU Lup	136-216	32	-7.70/-7.70	28	···	···	···	···	1
RW Aur	52-122	22	-7.50/-6.50	56	0.004	56	···	···	3

Continued on Next Page…

Table 6.2 – Continued

Star	EW$_{H\alpha}$	ref	log $\dot{M}$	ref	M_d	ref	i_d	ref	ID
RY Lup	7	32	···	···	···	···	···	···	2
SR 9	6–14	32	-8.26/-8.26	41	0.0019	8	···	···	2
St 34	78	31	-9.6/-9.6	57	<0.0005	6	···	···	4
SU Aur	2– 6	26	-8.30/-8.20	26	<0.0009	6	52	1	1
SX Cha	26	21	···	···	···	···	···	···	1
SY Cha	24–64	21	···	···	···	···	···	···	1
Sz 18	···	···	···	···	···	···	···	···	4
Sz 50	46	32	-10.30/-10.30	51	···	···	···	···	1
T Cha	2–10	32	···	···	···	···	···	···	2
TW Cha	26	21	···	···	···	···	···	···	1
TW Hya	194–220	10	-8.80/-8.80	28	···	···	7	45	2,4
UX Tau A	4	12	-9.00/-9.00	39	0.005	6	···	···	4
UY Aur	···	···	···	···	···	···	···	···	3
V1331 Cyg	41–59	22	···	···	0.5	40	···	···	3
V710 Tau	34–89	26	···	···	0.007	6	···	···	2
V853 Oph	41	49	-8.31/-8.31	41	···	···	···	···	2
VV Ser	22–90	22	-6.34/-6.34	24	···	···	81	19	2
VW Cha	60–147	21	···	···	···	···	···	···	1
VZ Cha	58–71	21	···	···	···	···	···	···	1
Wa Oph 6	35	49	-6.64/-6.64	7	0.081	8	41	7	1
WX Cha	65	21	···	···	···	···	···	···	1
XX Cha	133	21	···	···	···	···	···	···	1

References — (1) Akeson et al. 2005a (2) Akeson et al. 2005b (3) Alcala et al. 1995 (4) Alcala et al. 2000 (5) Andre et al. 1994 (6) Andrews & Williams 2005 (7) Andrews & Williams 2007a (8) Andrews & Williams 2007b (9) Andrews & Williams 2008 (10) Bary et al. 2003 (11) Barsony et al. 2005 (12) Beckwith et al. 1990 (13) Bontemps et al. 2001 (14) Brown et al. 2008 (15) Casanova et al. 1995 (16) Colavita et al. 2003 (17) D'Alessio et al. 2005 (18) Doucet et al. 2006 (19) Eisner et al. 2003 (20) Espaillat et al. 2007 (21) Feigelson et al. 1993 (22) Fernandez et al. 1995 (23) Furlan et al. 2006 (24) Garcia Lopez et al. 2006 (25) Greene & Meyer 1995 (26) Gudel et al. 2007a (27) Gudel et al. 2007b (28) Herczeg et al. 2008 (29) Hiramatsu et al. 2007 (30) Hughes et al. 1994 (31) Kenyon & Hartmann 1995 (32) Kessler-Silacci et al. 2006 (33) Kitamura et al. 2002 (34) Koerner & Sargent 1995 (35) Kudo et al. 2008 (36) Lahuis et al. 2007 (37) Luhman et al. 2004 (38) Luhman et al. 2007 (39) Najita et al. 2007 (40) Najita et al. 2009 (41) Natta et al. 2006 (42) Neuhauser et al. 1995 (43) Pinte et al. 2008 (44) Prato et al. 2003 (45) Qi et al. 2004 (46) Robrade et al. 2007 (47) Schneider et al. 2003 (48) Seperuelo Duarte et al. 2008 (49) Shevchenko et al. 1998 (50) Simon et al. 2001 (51) Spezzi et al. 2008 (52) Stapelfeldt et al. 1998 (53) Stelzer et al. 2004 (54) Thi et al. 2002 (55) Valenti et al. 2003 (56) Watson et al. 2009 (57) White et al. 2005

[*] Program ID: 1=Program 50641, 2=c2d, 3=Program 20363, 4=Program 30300

Table 6.3. Detection Statistics

	All [a]	No trans [b]	Trans [c]	P-value [d]
H I	0.53	0.51	0.67	0.19
H_2O	0.35	0.40	0.00	0.02
OH	0.49	0.55	0.00	0.00
HCN	0.46	0.51	0.00	0.00
C_2H_2	0.43	0.49	0.00	0.01
CO_2	0.47	0.53	0.00	0.00
[Ne II]	0.41	0.38	0.67	0.08
[Ar III]	0.46	0.54	0.00	0.00
H_2	0.30	0.33	0.11	0.15
Error	0.06	0.06	0.17	

[a] Fraction of disks with molecular/atomic detection (if wavelength region was observed)

[b] Fraction of non-transitional disks with molecular/atomic detection

[c] Fraction of transitional disks with molecular/atomic detection

[d] Probability of randomly sampling 8 disks with detection fraction given in column 4, assuming the population has the detection fraction given in column 2

[e] Error here and elsewhere assumes $\sigma = 1/(2\sqrt{N})$ where N is the number of objects observed in the sample.

Note. — Transitional disk subsample taken to be: CoKu Tau/4, CS Cha, DM Tau, GM Aur, HD 135344, LkHα 330, T Cha and UX Tau A.

Table 6.4. Parameter–Detection Statistics Correlations

	Hα	L_X	$\dot{M}$	$M_\star$	M_d	i	$L_\star$	H I	H_2O	OH	HCN	C_2H_2	CO_2	[Ne II]	[Ar III]	H_2
H I	**0.02**	0.34	0.06	0.03	0.39	-0.40	0.19	···	0.24	0.14	0.14	0.28	0.21	0.51	0.97	0.44
H_2O	0.15	-0.58	0.22	-0.16	-0.23	0.51	-0.18	0.23	···	**0.00**	**0.00**	**0.00**	**0.00**	0.71	**0.00**	**0.02**
OH	0.07	-0.57	0.23	-0.06	0.48	0.53	-0.08	0.15	**0.00**	···	**0.00**	**0.00**	**0.00**	0.61	**0.00**	**0.03**
HCN	0.13	-0.42	0.69	-0.07	-0.32	0.38	-0.11	0.14	**0.00**	**0.00**	···	**0.00**	**0.00**	0.97	**0.00**	**0.01**
C_2H_2	0.44	-0.27	0.06	**-0.02**	-0.57	0.57	-0.11	0.28	**0.00**	**0.00**	**0.00**	···	**0.00**	0.74	**0.00**	**0.02**
CO_2	0.08	-0.61	0.53	-0.09	-0.28	0.17	-0.13	0.21	**0.00**	**0.00**	**0.00**	**0.00**	···	0.26	**0.01**	0.15
[Ne II]	0.31	0.87	-0.48	-0.42	0.91	0.58	-0.23	0.51	-0.71	0.62	-0.97	0.74	0.26	···	0.17	0.43
[Ar III]	0.72	-0.94	0.63	-0.30	-0.40	0.27	-0.26	0.94	**0.00**	**0.00**	**0.00**	**0.00**	**0.00**	-0.18	···	**0.01**
H_2	0.62	-0.69	0.86	-0.21	0.20	0.58	-0.29	0.41	**0.01**	**0.02**	**0.01**	**0.01**	0.12	0.38	**0.00**	···

Note. — The absolute values of the numbers at upper right are the p-value associated with the slope of a linear regression of the two parameters. (There is a probability p of getting a slope at least that extreme by chance alone.) The sign gives the sense of the correlation (positive or negative). Lower-left quadrant shows the p-value associated with a chi-squared value for the two parameters (see text for details). p-values are bolded if ≤ 0.02.

Table 6.5: Colors

Star	n_{6-13}	n_{6-30}	n_{13-30}	Ref
AA Tau	-0.87	-0.73	-0.25	2, 4
AS 205 A	-0.37	-0.36	-0.35	1
AS 353 A	···	···	-0.65	1
BF Ori	-0.60	···	···	1
BP Tau	-0.67	-0.65	-0.34	2, 4
CHXR 30	···	···	-0.25	2, 4
CI Tau	-0.95	-0.56	-0.16	2, 4
CoKu Tau/4	-0.60	0.81	2.54	2, 4
CS Cha	···	···	2.95	1
CW Tau	-1.26	-0.77	-0.66	2, 4
CY Tau	-1.45	-1.20	-1.16	2, 4
DE Tau	-0.87	-0.49	0.01	2, 4
DG Tau	-0.20	-0.03	0.38	2, 4
DK Tau	-1.00	-0.80	-0.59	3
DL Cha	···	···	···	1
DL Tau	-0.78	-0.73	-0.68	2, 4
DM Tau	-0.11	0.60	1.40	2, 4
Do Ar 24E	2.26	0.89	-0.50	1
Do Ar 25	-1.45	···	···	1
DO Tau	-0.56	-0.33	-0.18	2, 4
DP Tau	-0.43	-0.41	-0.27	2, 4
DR Tau	-0.88	-0.63	-0.37	2, 4
EC 82	-0.26	0.11	0.49	1
EX Lup	2.13	0.69	-0.75	1
FN Tau	-0.29	-0.17	-0.01	2, 4
FT Tau	-0.62	-0.50	-0.32	2, 4
FX Tau	-1.05	-0.75	···	2, 4
FZ Tau	-1.14	···	-0.89	2
GI Tau	-0.55	-0.60	-0.70	2, 4
GK Tau	-0.45	-0.44	-0.28	2, 4
GM Aur	-0.91	0.48	1.95	2, 4
GQ Lup	-1.32	-0.74	-0.15	1
GW Lup	-0.56	···	···	1
Haro 1-16	-0.89	-0.02	0.85	1
Haro 1-17	-0.68	···	···	1
Haro 1-1	1.33	1.09	0.84	1
Haro 1-4	···	···	···	1
Haro 6-13	-0.56	0.08	0.55	2, 4
HD 101412	-0.67	···	···	1
HD 135344	···	···	1.67	1
HD 98922	···	···	-1.30	1
HK Tau	-0.72	0.06	1.03	2, 4
HN Tau	-0.70	-0.59	-0.58	2, 4
HQ Tau	-0.76	-0.66	-0.45	2, 4
HT Lup	0.10	-0.18	-0.47	1
IM Lup	-0.30	-0.29	-0.28	1
IQ Tau	-1.30	···	-0.59	2
LkCa 8	···	···	···	1
LkHa 270	-0.94	···	···	1
LkHa 326	-0.74	-0.29	0.17	1
LkHa 330	-1.51	0.21	1.96	1
LkHa 348	-1.13	-1.59	-2.05	1
RNO 15	-0.17	···	···	1
RNO 90	-0.88	-0.66	-0.44	1
RNO 91	···	0.13	···	1
ROXs 42C	-0.94	···	···	1
ROXs 43A	···	···	···	1
RR Tau	-0.84	···	···	1
RU Lup	0.74	0.09	-0.56	1
RW Aur	-0.67	-0.60	-0.47	2, 4
RY Lup	-1.04	···	···	1

Continued on Next Page...

Star	n_{6-13}	n_{6-30}	n_{13-30}	Ref
SR 9	-0.94	···	···	1
St 34	···	···	-0.52	1
SU Aur	-0.32	···	0.86	2
SX Cha	···	···	-0.47	2
SY Cha	···	···	-0.15	2
Sz 18	···	···	2.88	2
Sz 50	-0.49	-0.26	-0.03	1
T Cha	···	···	1.60	1
TW Cha	···	···	-0.10	1
TW Hya	0.37	0.54	0.72	3
UX Tau A	-1.99	-0.07	1.83	2, 4
UY Aur	···	···	-0.19	2, 4
V1331 Cyg	···	···	0.34	2, 4
V710 Tau	-1.07	-0.88	···	2, 4
V853 Oph	-1.41	···	···	1
VV Ser	-1.04	···	···	1
VW Cha	···	···	-0.11	1
VZ Cha	···	···	-1.05	1
Wa Oph 6	-1.00	-0.69	-0.38	1
WX Cha	···	···	-0.99	1
XX Cha	···	···	-0.25	1

References: (1) Evans et al. 2003 (2) Furlan et al. 2006 (3) Hartmann et al. 2005 (4) Watson et al. 2009

Table 6.6. Settling–Detection Statistics

	Region 1[a]	Region 2 [b]
H I	0.79	0.43
H_2O	0.79	0.19
OH	0.83	0.38
HCN	0.79	0.29
C_2H_2	0.71	0.14
CO_2	0.67	0.38
[Ne II]	0.42	0.52
[Ar III]	0.58	0.33
H_2	0.38	0.24
Error	0.20	0.22

[a] Detection fraction for Region 1 sources, with $n_{6-13} < -0.5$ and $n_{13-30} < 1$. Also see Figure 6.6.

[b] Detection fraction for Region 2 sources, with h $n_{6-13} > -0.5$ or $n_{13-30} > 1$

Table 6.7: Equivalent Widths

Star	H I (12.37)	H_2O (16.1)	H_2O (33)	OH (27.6)	HCN	C_2H_2	CO_2	[Ne II]	[Ar III]	H_2 (12.279)
AA Tau	21 ± 3	33 ± 3	168 ± 16	24 ± 17	82 ± 3	18 ± 2	35 ± 3	33 ± 3	16 ± 2	24 ± 3
AS 205 A	0 ± 0	8 ± 1	70 ± 7	2 ± 8	17 ± 2	6 ± 1	20 ± 1	0 ± 0	6 ± 1	0 ± 0
AS 353 A	20 ± 1	0 ± 0	0 ± 0	37 ± 10	0 ± 0	0 ± 0	15 ± 1	12 ± 1	0 ± 0	15 ± 1
BF Ori	27 ± 3	0 ± 0	···	···	0 ± 0	0 ± 0	0 ± 0	19 ± 3	···	0 ± 0
BP Tau	25 ± 3	30 ± 2	213 ± 15	26 ± 14	78 ± 3	10 ± 2	0 ± 0	0 ± 0	19 ± 1	8 ± 2
CHXR 30	0 ± 0	0 ± 0	0 ± 0	0 ± 0	0 ± 0	0 ± 0	0 ± 0	0 ± 0	0 ± 0	0 ± 0
CI Tau	24 ± 3	24 ± 2	102 ± 12	29 ± 13	32 ± 3	11 ± 2	17 ± 2	14 ± 2	0 ± 0	10 ± 2
CoKu Tau/4	0 ± 0	0 ± 0	0 ± 0	0 ± 0	0 ± 0	0 ± 0	0 ± 0	0 ± 0	0 ± 0	0 ± 0
CS Cha	116 ± 9	0 ± 0	0 ± 0	0 ± 0	0 ± 0	0 ± 0	0 ± 0	427 ± 7	0 ± 0	0 ± 0
CW Tau	28 ± 3	36 ± 2	197 ± 16	43 ± 17	24 ± 3	0 ± 0	25 ± 2	0 ± 0	17 ± 1	0 ± 0
CY Tau	19 ± 4	24 ± 4	107 ± 31	0 ± 0	34 ± 4	30 ± 2	21 ± 4	0 ± 0	0 ± 0	0 ± 0
DE Tau	0 ± 0	23 ± 2	24 ± 6	24 ± 7	14 ± 2	6 ± 1	9 ± 2	0 ± 0	0 ± 0	0 ± 0
DG Tau	0 ± 0	0 ± 0	0 ± 0	33 ± 7	0 ± 0	0 ± 0	0 ± 0	35 ± 1	0 ± 0	0 ± 0
DK Tau	32 ± 4	52 ± 3	279 ± 25	70 ± 24	41 ± 4	8 ± 2	13 ± 3	0 ± 0	15 ± 2	10 ± 3
DL Cha	0 ± 0	0 ± 0	···	···	0 ± 0	0 ± 0	44 ± 1	0 ± 0	···	0 ± 0
DL Tau	30 ± 2	0 ± 0	0 ± 0	24 ± 8	0 ± 0	23 ± 1	13 ± 2	17 ± 2	9 ± 1	0 ± 0
DM Tau	0 ± 0	0 ± 0	0 ± 0	0 ± 0	0 ± 0	0 ± 0	0 ± 0	100 ± 5	0 ± 0	61 ± 6
Do Ar 24E	0 ± 0	25 ± 2	96 ± 12	27 ± 13	37 ± 2	16 ± 1	15 ± 2	0 ± 0	7 ± 1	0 ± 0
Do Ar 25	0 ± 0	0 ± 0	···	···	89 ± 3	21 ± 2	0 ± 0	0 ± 0	···	141 ± 2
DO Tau	25 ± 2	0 ± 0	0 ± 0	37 ± 11	0 ± 0	0 ± 0	0 ± 0	0 ± 0	0 ± 0	0 ± 0
DP Tau	19 ± 3	24 ± 2	138 ± 16	32 ± 15	20 ± 3	2 ± 2	12 ± 2	18 ± 2	11 ± 1	19 ± 2
DR Tau	23 ± 2	20 ± 2	91 ± 8	12 ± 9	32 ± 2	6 ± 1	15 ± 2	0 ± 0	19 ± 1	0 ± 0
EC 82	0 ± 0	0 ± 0	0 ± 0	0 ± 0	0 ± 0	0 ± 0	0 ± 0	18 ± 2	0 ± 0	21 ± 2
EX Lup	22 ± 2	0 ± 0	0 ± 0	30 ± 10	0 ± 0	0 ± 0	0 ± 0	0 ± 0	11 ± 1	0 ± 0
FN Tau	0 ± 0	0 ± 0	0 ± 0	0 ± 0	0 ± 0	0 ± 0	0 ± 0	0 ± 0	0 ± 0	0 ± 0
FT Tau	26 ± 3	25 ± 3	121 ± 14	23 ± 15	39 ± 3	13 ± 2	27 ± 2	25 ± 2	13 ± 1	25 ± 3
FX Tau	0 ± 0	0 ± 0	···	···	0 ± 0	0 ± 0	0 ± 0	0 ± 0	···	0 ± 0
FZ Tau	27 ± 3	37 ± 3	221 ± 25	33 ± 26	26 ± 3	7 ± 2	44 ± 3	0 ± 0	34 ± 2	8 ± 2
GI Tau	0 ± 0	24 ± 2	182 ± 18	36 ± 17	38 ± 3	8 ± 2	0 ± 0	14 ± 2	15 ± 1	17 ± 2
GK Tau	0 ± 0	32 ± 3	121 ± 11	37 ± 9	0 ± 0	0 ± 0	0 ± 0	0 ± 0	9 ± 1	0 ± 0
GM Aur	142 ± 9	0 ± 0	0 ± 0	0 ± 0	0 ± 0	0 ± 0	0 ± 0	88 ± 7	0 ± 0	0 ± 0
GQ Lup	31 ± 3	28 ± 3	154 ± 11	25 ± 11	53 ± 3	9 ± 2	17 ± 3	0 ± 0	14 ± 1	0 ± 0
GW Lup	0 ± 0	0 ± 0	···	···	0 ± 0	29 ± 2	76 ± 3	0 ± 0	···	0 ± 0
Haro 1-16	35 ± 5	29 ± 3	70 ± 9	22 ± 9	26 ± 5	0 ± 0	0 ± 0	0 ± 0	0 ± 0	0 ± 0
Haro 1-17	0 ± 0	0 ± 0	···	···	0 ± 0	0 ± 0	0 ± 0	0 ± 0	···	51 ± 5
Haro 1-1	43 ± 4	0 ± 0	0 ± 0	0 ± 0	48 ± 4	0 ± 0	0 ± 0	0 ± 0	14 ± 1	11 ± 4
Haro 1-4	32 ± 3	0 ± 0	···	···	38 ± 3	20 ± 2	30 ± 2	13 ± 2	···	0 ± 0
Haro 6-13	17 ± 2	0 ± 0	0 ± 0	0 ± 0	0 ± 0	6 ± 1	26 ± 1	13 ± 1	0 ± 0	0 ± 0
HD 101412	9 ± 2	0 ± 0	···	···	0 ± 0	6 ± 1	23 ± 1	0 ± 0	···	0 ± 0
HD 135344	28 ± 1	0 ± 0	0 ± 0	0 ± 0	0 ± 0	0 ± 0	0 ± 0	0 ± 0	0 ± 0	0 ± 0
HD 98922	9 ± 1	0 ± 0	0 ± 0	0 ± 0	0 ± 0	0 ± 0	0 ± 0	0 ± 0	0 ± 0	0 ± 0
HK Tau	0 ± 0	0 ± 0	0 ± 0	0 ± 0	0 ± 0	0 ± 0	24 ± 2	20 ± 2	0 ± 0	13 ± 2
HN Tau	10 ± 2	26 ± 2	57 ± 6	7 ± 7	11 ± 2	0 ± 0	8 ± 2	16 ± 2	0 ± 0	0 ± 0
HQ Tau	0 ± 0	0 ± 0	0 ± 0	0 ± 0	0 ± 0	0 ± 0	0 ± 0	0 ± 0	0 ± 0	0 ± 0
HT Lup	0 ± 0	0 ± 0	0 ± 0	0 ± 0	0 ± 0	0 ± 0	24 ± 1	0 ± 0	0 ± 0	0 ± 0
IM Lup	0 ± 0	0 ± 0	0 ± 0	0 ± 0	0 ± 0	0 ± 0	26 ± 2	20 ± 2	0 ± 0	0 ± 0
IQ Tau	0 ± 0	18 ± 3	132 ± 12	4 ± 12	63 ± 4	16 ± 2	0 ± 0	27 ± 3	14 ± 1	0 ± 0
LkCa 8	69 ± 6	0 ± 0	···	···	0 ± 0	0 ± 0	0 ± 0	55 ± 5	···	0 ± 0
LkHa 270	0 ± 0	0 ± 0	···	···	0 ± 0	0 ± 0	42 ± 2	40 ± 2	···	27 ± 3
LkHa 326	0 ± 0	21 ± 2	36 ± 8	18 ± 9	12 ± 2	0 ± 0	23 ± 2	14 ± 2	6 ± 1	0 ± 0
LkHa 330	18 ± 2	0 ± 0	0 ± 0	0 ± 0	0 ± 0	0 ± 0	0 ± 0	0 ± 0	0 ± 0	0 ± 0
LkHa 348	27 ± 2	0 ± 0	0 ± 0	0 ± 0	0 ± 0	0 ± 0	0 ± 0	0 ± 0	0 ± 0	0 ± 0
RNO 15	0 ± 0	0 ± 0	···	···	0 ± 0	9 ± 1	0 ± 0	10 ± 1	···	0 ± 0
RNO 90	30 ± 3	18 ± 2	249 ± 17	26 ± 17	78 ± 3	14 ± 2	22 ± 2	0 ± 0	20 ± 1	13 ± 2
RNO 91	···	···	0 ± 0	22 ± 6	···	···	···	···	0 ± 0	···
ROXs 42C	0 ± 0	0 ± 0	···	···	0 ± 0	0 ± 0	0 ± 0	0 ± 0	···	0 ± 0
ROXs 43A	0 ± 0	0 ± 0	···	···	0 ± 0	0 ± 0	0 ± 0	0 ± 0	···	0 ± 0
RR Tau	4 ± 2	0 ± 0	···	···	0 ± 0	0 ± 0	0 ± 0	0 ± 0	···	0 ± 0
RU Lup	26 ± 2	0 ± 0	0 ± 0	16 ± 5	22 ± 2	0 ± 0	17 ± 2	14 ± 2	0 ± 0	0 ± 0
RW Aur	36 ± 3	32 ± 3	147 ± 15	28 ± 15	39 ± 3	14 ± 2	35 ± 3	0 ± 0	18 ± 1	22 ± 3

Continued on Next Page . . .

Star	H I (12.37)	H_2O (16.1)	H_2O (33)	OH (27.6)	HCN	C_2H_2	CO_2	[Ne II]	[Ar III]	H_2 (12.279)
RY Lup	0 ± 0	0 ± 0	···	···	0 ± 0	0 ± 0	0 ± 0	0 ± 0	···	0 ± 0
SR 9	0 ± 0	0 ± 0	···	···	0 ± 0	0 ± 0	0 ± 0	0 ± 0	···	28 ± 4
St 34	0 ± 0	0 ± 0	0 ± 0	0 ± 0	0 ± 0	0 ± 0	0 ± 0	0 ± 0	0 ± 0	0 ± 0
SU Aur	17 ± 2	0 ± 0	0 ± 0	0 ± 0	0 ± 0	0 ± 0	0 ± 0	12 ± 2	0 ± 0	0 ± 0
SX Cha	0 ± 0	19 ± 2	148 ± 16	21 ± 16	13 ± 2	−0 ± 1	0 ± 0	0 ± 0	11 ± 1	0 ± 0
SY Cha	0 ± 0	0 ± 0	0 ± 0	23 ± 14	30 ± 2	12 ± 1	29 ± 2	20 ± 2	10 ± 1	0 ± 0
Sz 18	0 ± 0	0 ± 0	0 ± 0	0 ± 0	0 ± 0	0 ± 0	0 ± 0	0 ± 0	0 ± 0	0 ± 0
Sz 50	0 ± 0	0 ± 0	0 ± 0	21 ± 8	32 ± 3	0 ± 0	43 ± 2	0 ± 0	7 ± 1	0 ± 0
T Cha	0 ± 0	0 ± 0	0 ± 0	0 ± 0	0 ± 0	0 ± 0	0 ± 0	24 ± 2	0 ± 0	0 ± 0
TW Cha	0 ± 0	41 ± 3	380 ± 30	36 ± 29	82 ± 4	22 ± 3	0 ± 0	0 ± 0	33 ± 2	24 ± 3
TW Hya	76 ± 3	0 ± 0	0 ± 0	0 ± 0	0 ± 0	0 ± 0	0 ± 0	48 ± 3	0 ± 0	0 ± 0
UX Tau A	92 ± 7	0 ± 0	0 ± 0	0 ± 0	0 ± 0	0 ± 0	0 ± 0	37 ± 5	0 ± 0	0 ± 0
UY Aur	19 ± 2	0 ± 0	0 ± 0	19 ± 11	29 ± 2	8 ± 1	28 ± 1	0 ± 0	9 ± 1	22 ± 2
V1331 Cyg	22 ± 2	0 ± 0	0 ± 0	29 ± 9	0 ± 0	0 ± 0	0 ± 0	0 ± 0	0 ± 0	14 ± 2
V710 Tau	90 ± 5	0 ± 0	···	···	95 ± 6	42 ± 3	59 ± 5	0 ± 0	···	0 ± 0
V853 Oph	0 ± 0	0 ± 0	···	···	29 ± 2	20 ± 1	21 ± 2	25 ± 2	···	0 ± 0
VV Ser	31 ± 2	0 ± 0	···	···	0 ± 0	0 ± 0	0 ± 0	0 ± 0	···	0 ± 0
VW Cha	51 ± 3	32 ± 2	163 ± 15	61 ± 16	34 ± 3	9 ± 2	22 ± 3	30 ± 3	12 ± 1	8 ± 3
VZ Cha	0 ± 0	40 ± 4	253 ± 30	40 ± 29	41 ± 4	15 ± 2	10 ± 4	0 ± 0	26 ± 2	0 ± 0
Wa Oph 6	5 ± 2	18 ± 2	63 ± 11	20 ± 12	14 ± 2	2 ± 1	17 ± 2	12 ± 2	0 ± 0	0 ± 0
WX Cha	43 ± 4	34 ± 4	457 ± 41	56 ± 38	67 ± 4	16 ± 2	27 ± 4	0 ± 0	27 ± 3	18 ± 3
XX Cha	0 ± 0	31 ± 3	145 ± 11	19 ± 12	43 ± 3	24 ± 2	41 ± 3	28 ± 3	19 ± 1	22 ± 3

Table 6.8. Parameter–Equivalent Width Correlations

	$H\alpha$	L_X [a]	$\log \dot{M}$[b]	$M_\star$	M_d	i	$L_\star$	H I[c]	H_2O [d]	H_2O [e]	OH	HCN[f]	C_2H_2 [f]	CO_2[g]	[Ne II][h]	[Ar III]	H_2 [i]
$H\alpha$	···	···	···	···	···	···	···	0.03	-0.01	-0.15	-0.14	-0.39	-0.01	0.19	0.29	0.23	0.01
L_X	···	···	···	···	···	···	···	0.27	0.47	0.43	0.25	0.05	-0.02	0.44	0.13	-0.04	-0.04
$\log \dot{M}$	···	···	···	···	···	···	···	-0.34	-0.36	-0.19	-0.18	-0.21	**-0.58**	-0.03	-0.45	-0.01	**-0.69**
$M_\star$	···	···	···	···	···	···	···	-0.16	-0.02	0.21	-0.08	-0.10	-0.18	0.18	-0.17	0.05	0.05
M_d	···	···	···	···	···	···	···	-0.06	-0.39	-0.31	-0.02	0.29	0.22	0.04	-0.15	-0.40	-0.11
i	···	···	···	···	···	···	···	-0.13	-0.05	-0.15	-0.31	0.20	0.09	0.45	-0.26	0.17	-0.20
$L_\star$	···	···	···	···	···	···	···	-0.13	-0.40	-0.22	-0.12	-0.13	-0.39	-0.02	-0.20	-0.27	-0.31
H I	0.85	0.38	-0.08	-0.46	-0.82	-0.62	-0.54	···	0.46	0.51	0.37	0.35	0.38	0.33	**0.92**	0.13	-0.27
H_2O	-0.97	0.06	-0.12	-0.94	-0.11	-0.90	-0.05	0.07	···	**0.61**	**0.76**	0.32	0.22	0.19	0.66	**0.53**	-0.09
H_2O	-0.45	0.09	-0.44	0.35	-0.22	-0.67	-0.29	0.04	**0.00**	···	**0.63**	**0.66**	0.28	0.26	0.61	**0.76**	0.01
OH	-0.41	0.32	-0.42	-0.69	-0.94	-0.33	-0.54	0.09	**0.00**	**0.00**	···	0.23	-0.01	-0.05	0.17	0.32	-0.45
HCN	-0.03	0.83	-0.39	-0.62	0.23	0.55	-0.51	0.13	0.10	**0.00**	0.20	···	**0.48**	0.29	**0.71**	**0.49**	0.15
C_2H_2	-0.94	-0.95	**-0.01**	-0.39	0.39	0.78	-0.05	0.12	0.31	0.20	-0.98	**0.01**	···	0.33	0.45	0.22	0.50
CO_2	0.32	0.10	-0.91	0.40	0.86	0.20	-0.94	0.15	0.40	0.24	-0.81	0.13	0.10	···	**0.68**	0.20	0.42
[Ne II]	0.12	0.68	-0.06	-0.46	-0.61	-0.40	-0.37	**0.00**	0.03	0.05	0.52	**0.00**	0.10	**0.00**	···	0.62	**0.92**
[Ar III]	0.28	-0.88	-0.96	0.84	-0.16	0.69	-0.21	0.65	**0.01**	**0.00**	0.10	**0.01**	0.32	0.40	0.06	···	-0.08
H_2	0.95	-0.90	**-0.02**	0.88	-0.73	-0.71	-0.24	-0.36	-0.75	0.98	-0.07	0.59	0.06	0.11	**0.00**	-0.78	···

Note. — Upper-right quadrant shows the correlation coefficient, R, between the two parameters. Lower-left quadrant shows the p-value, p, associated with the slope of a linear regression of the two parameters. Both R and p are bolded if $p \leq 0.02$.

[a] Outliers VW Cha and SU Aur excluded

[b] Outlier Sz 50 excluded

[c] Outliers VW Cha, WX Cha and V710 Tau excluded

[d] 16.1 μm

[e] 33 μm

[f] Outlier V710 Tau excluded

[g] Outliers V710 Tau and GW Lup excluded

[h] Outlier CS Cha excluded

[i] Outlier DoAr 25 excluded

Table 6.9. Color–Equivalent Width Relationships

	H I	H_2O	H_2O	OH	HCN	C_2H_2	CO_2	[Ne II]	[Ar III]	H_2
n_{6-13}	-0.56	-0.32	-0.42	-0.50	-0.13	-0.06	-0.86	0.98	-0.03	-0.25
n_{13-30}	**0.00**	-0.40	-0.03	-0.25	-0.74	-0.04	0.58	**0.00**	-0.05	0.03
n_{6-30}	0.04	**-0.02**	**-0.00**	-0.20	**-0.01**	-0.04	-0.65	**0.00**	**-0.00**	**0.01**

Note. — Absolute values shown are p-value associated with the slope of a linear regression of the two parameters. Signs show whether the correlation is positive or negative.

Table 6.10. Model Fit Parameters

Source	T [K]	Area [AU^2]	N$_{H_2O}$ [cm^{-2}]	N$_{CO_2}$ [cm^{-2}]	N$_{HCN}$ [cm^{-2}]	$N_{C_2H_2}$ [cm^{-2}]	T [K]	Area [AU^2]	N$_{OH}$ [cm^{-2}]
AA Tau	400	1.76	4.E+18	8.E+15	2.E+16	2.E+15	1100	11.00	4.E+14
AS 205 A	600	3.14	6.E+19	2.E+16	4.E+16	8.E+15	1200	12.57	4.E+15
AS 353 A	···	···	···	2.E+16	···	···	800	0.63	1.E+19
BP Tau	500	5.03	1.E+18	···	1.E+16	1.E+15	1000	31.42	6.E+14
CI Tau	600	0.44	1.E+19	1.E+16	2.E+16	4.E+15	1100	11.00	6.E+14
CW Tau	500	3.50	4.E+18	8.E+15	8.E+15	···	1100	13.98	2.E+15
CY Tau	900	0.03	6.E+19	4.E+16	4.E+16	4.E+16	0	0.00	···
DE Tau	600	0.11	8.E+19	2.E+16	4.E+16	1.E+16	1200	11.00	2.E+14
DG Tau	···	···	···	···	···	···	1200	13.98	8.E+15
DK Tau	500	2.75	4.E+18	4.E+15	1.E+16	2.E+15	1000	11.00	2.E+15
DL Cha	···	···	···	1.E+21	···	···	···	···	···
DL Tau	···	···	···	···	···	2.E+16	600	0.44	4.E+20
Do Ar 24E	500	2.75	1.E+19	1.E+16	2.E+16	8.E+15	1200	11.00	2.E+15
Do Ar 25	···	···	···	···	2.E+16	4.E+15	···	···	···
DO Tau	···	···	···	···	···	···	800	1.26	1.E+19
DP Tau	400	1.76	4.E+19	6.E+15	8.E+15	1.E+15	1100	11.00	1.E+15
DR Tau	600	1.76	8.E+18	1.E+16	2.E+16	4.E+15	1200	11.00	1.E+15
EX Lup	···	···	···	···	···	···	800	1.13	2.E+19
FT Tau	300	1.13	4.E+20	1.E+16	2.E+16	2.E+15	1200	3.14	1.E+15
FZ Tau	500	1.76	2.E+19	1.E+16	8.E+15	2.E+15	800	11.00	2.E+15
GI Tau	400	2.75	6.E+18	···	1.E+16	2.E+15	1200	2.75	2.E+15
GK Tau	300	1.76	8.E+21	···	···	···	1200	11.00	8.E+14
GQ Lup	500	5.11	4.E+17	4.E+15	6.E+15	1.E+15	1200	5.11	2.E+15
GW Lup	···	···	···	1.E+16	···	4.E+15	···	···	···
Haro 1-16	300	2.75	1.E+21	···	1.E+16	···	1200	11.00	8.E+14
Haro 1-1	···	···	···	···	4.E+16	···	···	···	···
Haro 1-4	···	···	···	2.E+16	2.E+16	8.E+15	···	···	···
Haro 6-13	···	···	···	6.E+16	···	1.E+16	···	···	···
HD 101412	···	···	···	1.E+17	···	2.E+16	···	···	···
HK Tau	···	···	···	8.E+15	···	···	···	···	···
HN Tau	700	0.11	4.E+20	1.E+17	6.E+16	···	1100	11.00	6.E+14
HT Lup	···	···	···	2.E+17	···	···	···	···	···
IM Lup	···	···	···	2.E+16	···	···	···	···	···
IQ Tau	700	0.10	6.E+19	···	8.E+16	2.E+16	700	9.82	8.E+14
LkHa 270	···	···	···	2.E+16	···	···	···	···	···
LkHa 326	700	0.10	4.E+19	2.E+16	1.E+16	···	600	0.88	8.E+16
RNO 15	···	···	···	···	···	1.E+16	···	···	···
RNO 90	700	2.93	2.E+18	6.E+15	2.E+16	4.E+15	1100	11.70	4.E+15
RNO 91	···	···	···	···	···	···	900	1.13	4.E+20
RU Lup	···	···	···	6.E+17	2.E+18	···	900	0.59	4.E+19
RW Aur	500	10.60	1.E+19	2.E+16	2.E+16	4.E+15	1000	42.41	2.E+15
SX Cha	300	1.76	8.E+20	···	6.E+15	2.E+14	1200	11.00	4.E+14
SY Cha	···	···	···	6.E+15	8.E+15	2.E+15	700	0.11	4.E+19
Sz 50	···	···	···	1.E+16	1.E+16	···	700	0.11	4.E+19
TW Cha	500	1.02	1.E+18	···	6.E+15	1.E+15	1100	1.82	2.E+15
UY Aur	···	···	···	2.E+17	4.E+17	6.E+16	900	0.99	1.E+19
V1331 Cyg	···	···	···	···	···	···	800	0.44	2.E+19
V710 Tau	···	···	···	1.E+16	1.E+16	4.E+15	···	···	···
V853 Oph	···	···	···	1.E+16	2.E+16	6.E+15	700	0.20	6.E+20
VW Cha	500	4.91	2.E+18	6.E+15	8.E+15	2.E+15	900	19.63	4.E+15
VZ Cha	600	0.79	1.E+19	8.E+15	2.E+16	6.E+15	1200	19.63	4.E+14
Wa Oph 6	600	0.82	2.E+19	2.E+16	1.E+16	2.E+15	1100	20.42	8.E+14
WX Cha	500	1.77	4.E+18	6.E+15	1.E+16	2.E+15	1000	19.63	4.E+14
XX Cha	200	1.76	1.E+22	2.E+16	6.E+16	2.E+16	700	11.00	8.E+14